

UNIVERSITY OF GAZIANTEP
GRADUATE SCHOOL OF
NATURAL & APPLIED SCIENCES

PARTICLE IDENTIFICATION WITH THE ATLAS TRT

M. Sc. THESIS
IN
ENGINEERING PHYSICS

BY
ELİF KOLUMAN
JUNE 2011

Particle Identification with the ATLAS TRT

M.Sc. Thesis
in
Engineering Physics
University of Gaziantep

Supervisor
Assoc. Prof. Dr. Ayda Beddall

by
Elif Koluman
June 2011

T.C.
UNIVERSITY OF GAZIANTEP
GRADUATE SCHOOL OF
NATURAL & APPLIED SCIENCES
DEPARTMENT of ENGINEERING PHYSICS

Name of the thesis: Particle identification with the ATLAS TRT


Name of the student: Elif Koluman

Exam date: 27/06/2011

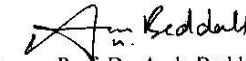
Approval of the Graduate School of Natural and Applied Sciences


Prof. Dr. Ramazan Koç
Director

I certify that this thesis satisfies all the requirements as a thesis for the degree of Master of Science.

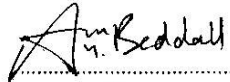

Prof. Dr. Necmeddin Yazıcı
Head of Department

This is to certify that we have read this thesis and that in our opinion it is fully adequate, in scope and quality, as a thesis for the degree of Master of Science.



Assoc. Prof. Dr. Ayda Beddall
Supervisor

Examining Committee Members

Assoc. Prof. Dr. Ayda Beddall


.....


Assist. Prof. Dr. Ahmet Bingül


.....

Assist. Prof. Dr. Andrew Beddall


.....

Assist. Prof. Dr. Rabia Güler Yıldırım


.....

Assist. Prof. Dr. Hümbet Ahmedov


.....

ABSTRACT

Particle Identification with the ATLAS TRT

KOLUMAN, Elif

M.Sc. in Engineering Physics

Supervisor: Assoc. Prof. Dr. Ayda Beddall

June 2011, 60 pages

This study compares three methods for the analysis electron-pion separation using the Transition Radiation Tracker in the ATLAS

In this study, the dalitz decay channel of neutral pion is selected using electron identification based on a simplified simulation of the TRT response to electrons and pions. A study of alternative treatments of high threshold information is performed to determine the most optimal approach to particle ID using the TRT detector. A chi approach is found to give the best signal significance in this decay channel.

Key Words: transition radiation, transition radiation tracker, particle identification, e/π separation, the high-threshold, the low-threshold, LHC, ATLAS.

ÖZET

ATLAS TRT ile Parçacık Analizi

KOLUMAN Elif

Yüksek Lisans Tezi, Fizik Müh. Bölümü

Tez Yöneticisi: Doç. Dr. Ayda BEDDALL

Haziran 2011, 60 sayfa

Bu çalışma, ATLAS-TRT (Transition Radiation Tracker) kullanılarak elektron piyon analizi için üç metot karşılaştırılmak üzere yapıldı.

Bu çalışmada, Elektronlar ve piyonlar, TRT’de basit bir simülasyon esas alınarak, elektron analizi yapılmak üzere nötr piyonun bozunum kanalları (dalitz decay channel) seçildi.

Yüksek eşik bilgisinine alternatif olarak daha iyi sonuçlara ulaşılabilmesi için, TRT dedektöründe, parçacık analizi için en uygun yaklaşım yapıldı. Bu üç ayrı metotun sonuçlarının yaklaşık olarak birbirine yakın olduğu gözlemlendi.

Bu bozunum kanalı için kullanılan bu üç metottan en iyi sinyal chi yaklaşımında görüldü.

Key words : geçiş radyasyonu, geçiş radyasyonu dedektörü, parçacık analizi, e/π analizi, yüksek eşik, alçak eşik, LHC, ATLAS.

ACKNOWLEDGMENTS

I would like to express my special thanks to my supervisor Assoc. Prof. Dr Ayda BEDDALL for her recommends and suggestions during the preparation of this thesis.

I also give my special thanks to Andrew Beddall and Ahmet Bingül due to their supports during the present work.

I thank Zekeriya UYSAL and Yılmaz DURMAZ due to their supports during the present work.

My special thanks also go to my family for their faithfully and unshakeable supports in the whole of my education life.

CONTENTS

ABSTRACT.....	i
ÖZET	ii
ACKNOWLEDGMENTS	iii
CONTENTS.....	iv
LIST OF FIGURES	vii
CHAPTER 1.....	1
1. Introduction.....	1
CHAPTER 2.....	15
2. Particle Identification.....	3
2.1. Ionization.....	3
2.2. Transition Radiation	6
2.3. Time of flight	8
2.4. Cherenkov Radiation.....	9
CHAPTER 3.....	12
3. The LHC and the ATLAS Experiment	12
3.1. The Large Hadron Collider (LHC)	12
3.1.1.The LHC Purpose	13
3.1.2.The design of the LHC.....	14
3.1.3.The LHC experiments.....	16

3.1.3.1.ALICE.....	17
3.1.3.2.ATLAS.....	18
3.1.3.3.CMS.....	18
3.1.3.4.LHCb.....	19
3.1.3.5.TOTEM.....	20
3.1.3.6.LHCf.....	21
3.2. ATLAS	21
3.2.1.The ATLAS experiment.....	22
3.2.1.1.The Inner Detector.....	24
3.2.1.1.1.The Pixel Detector.....	25
3.2.1.1.2.The SCT	26
3.2.1.1.3.The TRT.	26
3.2.1.2.Calorimeters.....	27
3.2.1.3.The Muon System.....	28
3.2.1.4.The magnet system.....	30
3.2.1.5.Triggering.....	30
CHAPTER 4.....	33
4. The Transition Radiation Tracker	33
4.1. Detector Description	33
4.2. Expected performance of the TRT	35
4.3. The TRT straw drift-tube	36
4.4. Gas composition	37
4.5. Barrel Modules	38

4.6. End-cap wheels	40
CHAPTER 5.	41
5. Particle Identification With The TRT	41
5.1. Cluster-counting technique	41
5.2. Time-over-threshold method	44
CHAPTER 6.	46
6. PID Case Study: Dalitz Decay Of The Neutral Pion	46
6.1. Introduction.	46
6.2. Data	47
6.2.1. FAWP	47
6.3. Analysis.	49
CHAPTER 7.	59
7. Summary And Conclusion	59
REFERENCES	60

LIST OF FIGURES

Figure 2.1. The energy loss curves as a function of momentum for different particles and for different materials. Source [4].	5
Figure 2.2. Fractional energy loss per radiation length as a function of electron or positron energy. Source [4].	6
Figure 2.3. Overview of the Transition Radiation	7
Figure 3.1. Overview of the LHC. Source [11]	16
Figure 3.2. Overview of the ALICE. Source [12].	17
Figure 3.3. Overview of the CMS. Source [13].	18
Figure 3.4. Overview of the LHCb. Source [14]	19
Figure 3.5. Overview of the ATLAS detector, Source [15].	23
Figure 3.6. The structure of the Inner Detector. Source [15].	25
Figure 3.7. The structure of the Inner Detector barrel. Source [15]	26
Figure 3.8. top: Overview of the calorimeter systems. Bottom: The structure of the LAr calorimeter. Source [15]	27
Figure 3.9. Overview of the Muon System. Source [15].	28
Figure 3.10. Overview of the ATLAS triggering scheme. Source [16].	31
Figure 4.1. Schematic 3D-view of the TRT. Source [17].	33
Figure 4.2. Schematic view of the TRT detector in the R-z plane. The main dimension of the detector are shown on the left (resp. right) hand side for the active detector volume (resp. the physical detector envelopes). Units are in mm. source [4].	34
Figure 4.3. $Bd0 \rightarrow j\psi Ks0$ simulated event display in the Inner Detector	36
Figure 4.4. Total predicted charge-collection time in a magnetic field of 2T as a function of the CF4 concentration for straws with a gas mixture containing 70% Xe and at their nominal gas gain of 2.5.104. The remainder of the gas is CO2.	

Source [4].....	38
Figure 4.5. A view of a barrel module	39
Figure 4.6. Layout of the barrel	39
Figure 4.7. High voltage test stand with several end-cap wheels under high voltage. Source[18].....	40
Figure 5.1. Pion misidentification probability as a function of the electron efficiency at 20GeV, as measured using an end-cap sector prototype. The probabilities to observe a given number of TR-clusters for pions and electrons are shown in the top left-hand corner. source [4]	42
Figure 5.2. Display of a simulated $B_d^0 \rightarrow J/\psi K_S^0$ event in the ATLAS barrel TRT at low luminosity. Reconstructed tracks are drawn as lines only up to a radius of 50 cm so as not to obscure the TRT hits. The small box selects a part of a pion track from the K_S^0 decay and of an electron track from a J/ψ decay. source [4]	43
Figure 5.3. Expanded view of the portion of the tracks within the box in Fig. 5.2. The electron track contains many more high-threshold hits (larger points) than the pion track. Electron identification via transition radiation is based on this difference. source [4]	43
Figure 5.4. Bethe-Bloch curves for various particles in the ATLAS TRT gas mixture. For the energy range of interest for the TRT, electrons are always on the Fermi plateau, while hadrons are on the relativistic rise up to very large momentum.Source [4].....	44
Figure 5.5. Dependence of the time-over-threshold on the track distance, y , from the wire. The straw signal is shown before and after the low-threshold (200 eV) discrimination. Source[4].....	45
Figure 6.1. Pion decay mode.....	46
Figure 6.2. number of low level hits, n_{lt} , as simulated by FAWP.....	48
Figure 6.3. High threshold probability as a function of the gamma-factor. The curve is a fit to test beam data.....	49
Figure 6.4. Distribution of the number of high threshold hits, n_{ht} , for pions and electrons in the FAWP simulation of the TRT with equal number of electrons and pion	49

Figure 6.5. Distribution of the number of high threshold hits, n_{ht} , for pions and electrons.	50
Figure 6.6. Distribution of the number of high threshold hits divided by the number of low threshold hits, n_{ht}/n_{lt}	51
Figure 6.7. Distribution of χ	52
Figure 6.8. The reconstructed Dalitz signal with increasing cuts on n_{ht}	53
Figure 6.9. The reconstructed Dalitz signal with increasing cuts on n_{ht}/n_{lt}	54
Figure 6.10. The reconstructed Dalitz signal with increasing cuts on χ	55
Figure 6.11. Purity, efficiency and their product for increasing cuts on n_{ht}	56
Figure 6.12. Purity, efficiency and their product for increasing cuts on n_{ht}/n_{lt}	57
Figure 6.13. Purity, efficiency and their product for increasing cuts on χ	58

CHAPTER 1

1.Introduction

The Transition Radiation Tracker (TRT)[1] is a part of the Inner Detector of the ATLAS experiment[2]. It is designed to provide powerful pattern recognition capabilities and electron identification via transition radiation.

The TRT is a straw drift-tube detector, with a central barrel section and two end-cap sides, giving an average of 35 crossed straws per track. In the barrel TRT, axial straws are embedded in fibre radiators, while, in the end-caps, layers of radial straws alternate with foil radiators. These geometries have been chosen in order to have an approximately constant number of straws crossed by charged particles with $p_T > 0.5$ GeV over the full rapidity coverage ($|\eta| < 2.5$). Transition radiation is produced when a charged ultra-relativistic particle crosses the interface between different media, mainly polypropylene (fibres or foils) and air in the case of the TRT. The transition-radiation photons are emitted at very small angle with respect to the parent-particle trajectory and are therefore most often detected in the same straws as those crossed by the parent particle.

The TRT straw drift-tubes provide two types of information: the distance of closest approach of the track to the anode wire (for tracking purposes via drift-time measurements) and the energy deposited in the straw (for particle identification). This energy deposition is the sum of the ionisation losses of the charged particle crossing the straw and of the usually larger energy depositions due to transition-radiation photon absorption. The low-threshold discriminator level is set to a nominal value of 200 eV, which is safely above the noise level ($\sigma \sim 40$ eV) and significantly below the average energy loss of ~ 2 keV, expected for minimum-ionising particles traversing the straw gas. With this low-threshold setting, the front-end electronics detects the initial ionisation cluster for precise drift-time determination. The high-

threshold discriminator level is set to a nominal value of 5 keV, which is optimised for e/π separation. Particle identification studies based on the cluster-counting technique with different TRT prototypes have been reported in [3].

In this thesis a study of electron identification algorithms is made by using a simple simulation of the ATLAS TRT.

Chapter 2 describes the general principles of particle identification in High Energy Physics. The LHC and its experiments are described in Chapter 3 with more emphasis on ATLAS while the TRT is described in more detail in Chapter 4. The method of particle ID with the ATLAS TRT are described in Chapter 5 followed by a case study in Chapter 6 where LHC collisions are simulated with Pythia and passed through a toy Monte Carlo simulation of the TRT response. In this case study particle identification algorithms are applied in the reconstruction of the Dalitz Decay of the Neutral Pion.

CHAPTER 2

2. Particle Identification

In this chapter a general overview is given of particle identification methods commonly used in High Energy Physics.

2.1. Ionization

Charged particles lose energy continuously by interacting with matter. Moderately relativistic charged particles other than electrons lose energy primarily by ionization. The mean energy loss is given by the Bethe-Bloch function[4];

$$-\left(\frac{dE}{dx}\right) = Kz^2 \frac{Z}{A} \frac{1}{\beta^2} \left[\frac{1}{2} \ln \left(\frac{2(\beta\gamma c)^2 m_e T_{\max}}{I^2} \right) - \beta^2 - \frac{\delta}{2} \right] \quad (2.1)$$

where T_{\max} is the maximum kinetic energy which can be imparted to a free electron in a single collision.

$$T_{\max} = 2m_e(c\beta\gamma)^2 \quad (2.2)$$

This latter formula is valid for $\frac{2m_e\gamma}{M} \ll 1$; at the highest energy T_{\max} has a small dependence on M , the incident particle mass, but for all practical purposes in high

energy physics $\frac{dE}{dx}$ in a given material depends only on β . The variables used in the

previous formulae are defined in Tab. 2.1. The Bethe-Bloch curves are shown in Fig. 2.1 for different materials. The energy loss decreases with increasing momentum

as $\frac{1}{\beta^2}$ at low momentum, and reaches a minimum at $\beta\gamma \sim 3$. Above that point, the energy loss rises logarithmically in the so-called relativistic rise region, until it saturates (at the so-called ‘Fermi plateau’). The relativistic rise is limited by the

polarization of the media, which depends on the electron density. For gases, which have a low electron density, the relativistic rise is fairly high. For Xenon, as an example, the relativistic rise is around 75%. The Bethe-Bloch formula describes just the mean energy loss. The distribution of the energy loss is Gaussian for thick layers,

Table 2.1: Summary of the variables used in this Section. Source [4].

Symbol	Definition	Units or Value
α	Fine structure constant ($e^2/4\pi\epsilon_0\hbar c$)	1/137.035 999 76(50)
M	Incident particle mass	MeV/ c^2
E	Incident particle energy $\gamma M c^2$	MeV
T	Kinetic energy	MeV
$m_e c^2$	Electron mass $\times c^2$	0.510 998 902(21) MeV
r_e	Classical electron radius $e^2/4\pi\epsilon_0 m_e c^2$	2.817 940 285(31) fm
N_A	Avogadro's number	$6.022 141 99(47) \times 10^{23} \text{ mol}^{-1}$
ze	Charge of incident particle	
Z	Atomic number of medium	
A	Atomic mass of medium	g mol^{-1}
K/A	$4\pi N_A r_e^2 m_e c^2 / A$	0.307 075 MeV $\text{g}^{-1} \text{cm}^2$ for $A = 1 \text{ g mol}^{-1}$
I	Mean excitation energy	eV (<i>Nota bene!</i>)
δ	Density effect correction to ionization energy loss	
$\hbar\omega_p$	Plasma energy ($\sqrt{4\pi N_e r_e^3 m_e c^2 / \alpha}$)	$28.816 \sqrt{\rho(Z/A)} \text{ eV}^{(a)}$
N_e	Electron density	(units of r_e) $^{-3}$
w_j	Weight fraction of the j th element in a compound or mixture	
n_j	α number of j th kind of atoms in a compound or mixture	
X_0	Radiation length	g cm^{-2}
—	$4\alpha r_e^2 N_A / A$	$(716.408 \text{ g cm}^{-2})^{-1}$ for $A = 1 \text{ g mol}^{-1}$
E_c	Critical energy	MeV
E_s	Scale energy $\sqrt{4\pi/\alpha} m_e c^2$	21.2052 MeV
R_M	Molière radius	g cm^{-2}

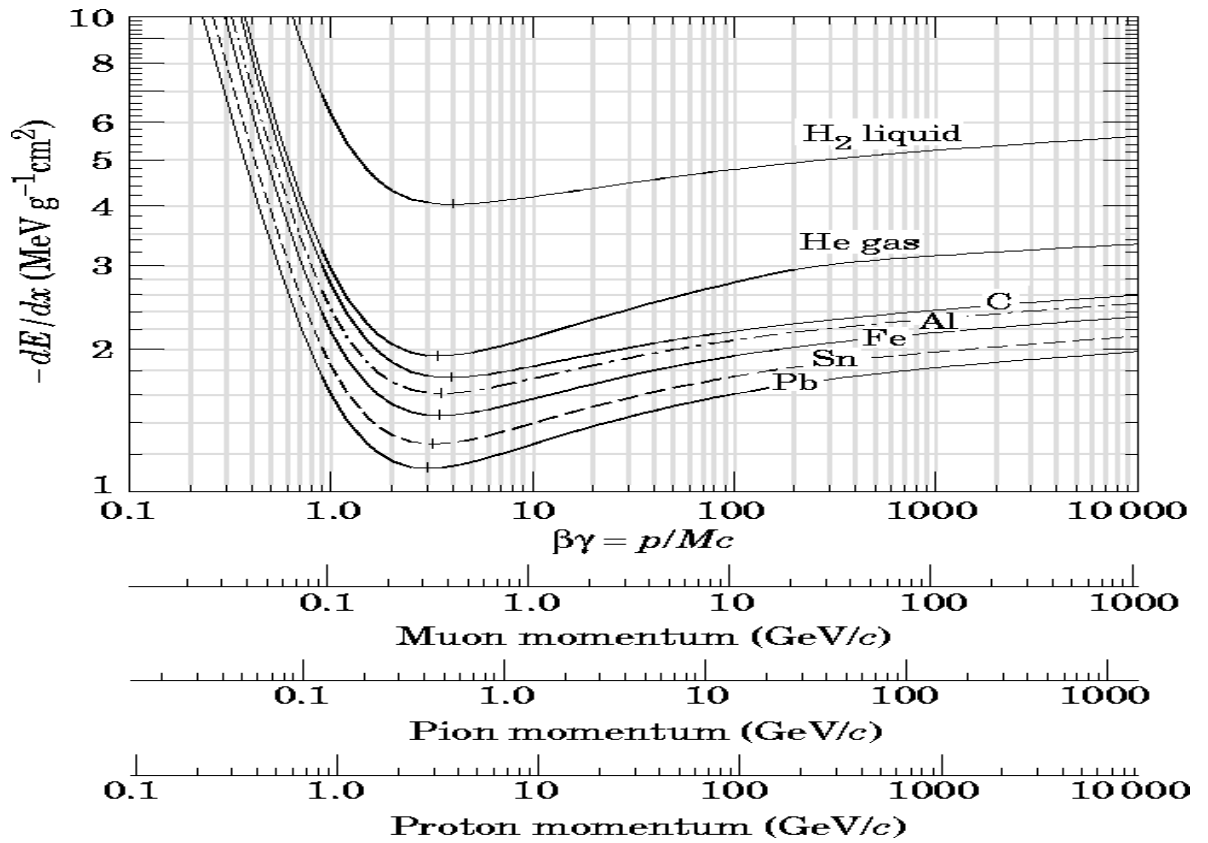


Figure 2.1. The energy loss curves as a function of momentum for different particles and for different materials. Source [4].

while it follows the so-called Landau distribution in the case of thin layers. Big fluctuations in the energy loss, in this latter case, cause the typical high-energy tail of the distribution (the Landau tail), which is due to knock-on electrons, or δ -rays. Electrons, on the other hand, at low energy lose energy primarily by ionization, but as the energy increases bremsstrahlung becomes more important, as shown in Fig. 2.2. Ionization loss by electrons differs from loss by heavy particles because of kinematics, spin and the identity of the incident electron with the electrons which it ionizes. While ionization losses rise logarithmically with energy, bremsstrahlung losses rise nearly linearly and dominate above a few tens of MeV in most materia

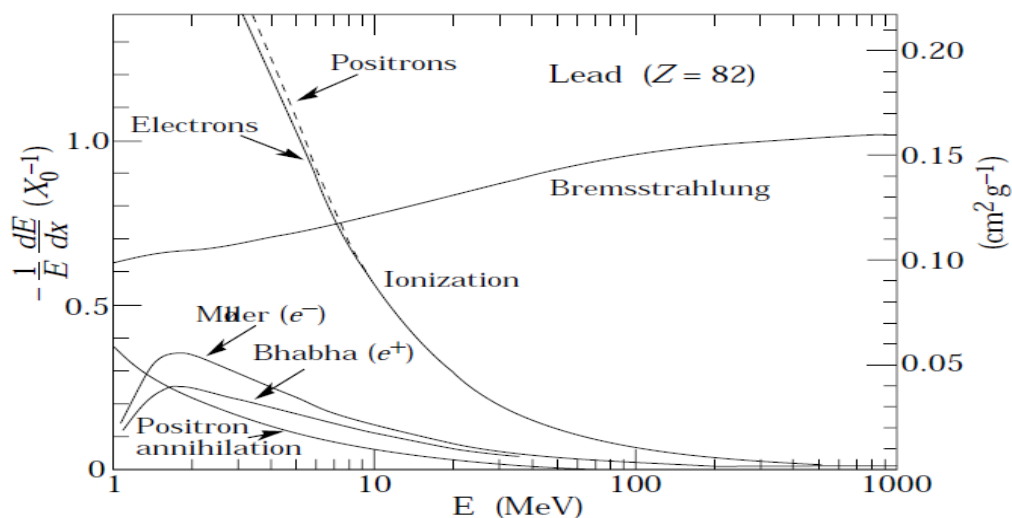


Figure 2.2. Fractional energy loss per radiation length as a function of electron or positron energy. Source [4].

2.2. Transition Radiation

Transition radiation is produced by relativistic charged particles when they cross the interface of two media of different dielectric constants (show Figure 2.3). The emitted radiation is the homogeneous difference between the two inhomogeneous solutions of Maxwell's equations of the electric and magnetic fields of the moving particle in each medium separately. In other words, since the electric field of the particle is different in each medium, the particle has to "shake off" the difference when it crosses the boundary. The total energy loss of a charged particle on the transition depends on its Lorentz factor $\gamma = E / mc^2$ and mostly directed forward, peaking at an angle of the order of $1 / \gamma$ relative to the particle's path. The intensity of the emitted radiation is roughly proportional to the particle's energy E .

Optical transition radiation is emitted both in the forward direction and reflected by the interface surface. In case of a foil having an angle at 45 degrees with respect to a particle beam, the particle beam's shape can be visually seen at an angle of 90 degrees. More elaborate analysis of the emitted visual radiation may allow for the determination of γ and emittance.

The characteristics of this electromagnetic radiation makes it suitable for particle discrimination, particularly of electrons and hadrons in the momentum range between $1\text{GeV} / c$ and $100\text{GeV} / c$. The transition radiation photons produced by electrons have wavelengths in the X-ray range, with energies typically in the range from 5 to 15keV. However, the number of produced photons per interface crossing is very small: for particles with $\gamma = 2 \times 10^3$, about 0.8 X-ray photons are detected. Usually several layers of alternating materials or composites are used to collect enough transition radiation photons for an adequate measurement—for example, one layer of inert material followed by one layer of detector (e.g. microstrip gas chamber), and so on [5].

By placing interfaces (foils) of very precise thickness and foil separation, coherence effects will modify the transition radiation's spectral and angular characteristics. This gives rise to a much higher number of photons in a smaller angular "volume". Applications of this x-ray source are limited by the fact that the radiation is emitted in a cone, with a minimum intensity at the center. X-ray focusing devices (crystals/mirrors) are not easy to build for such radiation patterns.

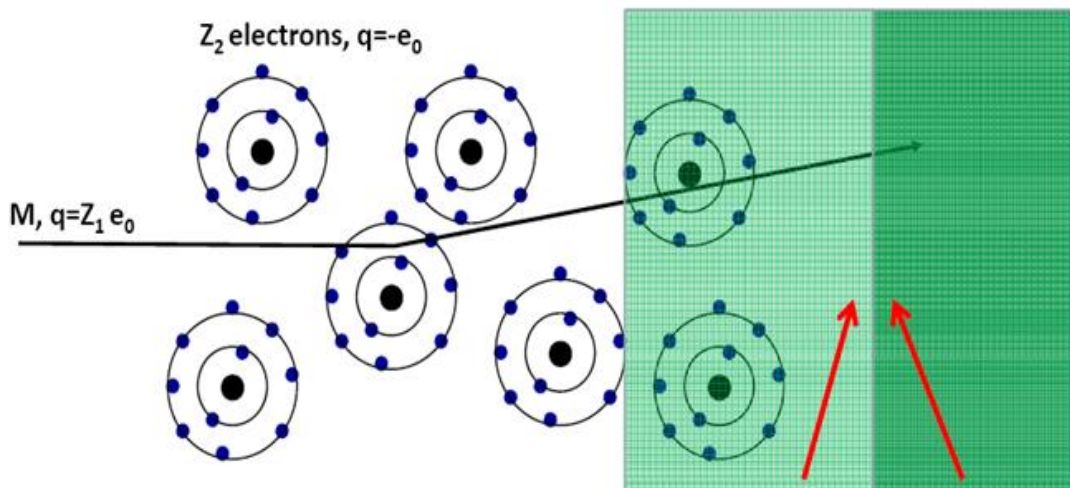


Figure 2.3. Overview of the Transition Radiation

2.3. Time of flight

Time of flight (TOF) describes a variety of methods that measure the time that it takes for an object, particle or acoustic, electromagnetic or other wave to travel a distance through a medium. This measurement can be used for a time standard (such as an atomic fountain), as a way to measure velocity or path length through a given medium, or as a way to learn about the particle or medium (such as composition or flow rate). The traveling object may be detected directly (e.g., ion detector in mass spectrometry) or indirectly (e.g., light scattered from an object in laser doppler velocimetry) [6].

- In time-of-flight mass spectrometry ions are accelerated by an electrical field to the same kinetic energy with the velocity of the ion depending on the mass-to-charge ratio. Thus the time-of-flight is used to measure velocity, from which the mass-to-charge ratio can be determined. The time-of-flight of electrons is used to measure their kinetic energy [7].
- In near infrared spectroscopy, the TOF method is used to measure the media-dependent optical pathlength over a range of optical wavelengths, from which composition and properties of the media can be analyzed [8].
- In ultrasonic flow meter measurement, TOF is used to measure speed of signal propagation upstream and downstream of flow of a media, in order to estimate total flow velocity. This measurement is made in a collinear direction with the flow.
- In planar Doppler velocimetry (optical flow meter measurement), TOF measurements are made perpendicular to the flow by timing when individual particles cross two or more locations along the flow (collinear measurements would require generally high flow velocities and extremely narrow-band optical filters).
- In optical interferometry, the pathlength difference between sample and reference arms can be measured by TOF methods, such as frequency modulation followed by phase shift measurement or cross correlation of

- signals. Such methods are used in laser radar and laser tracker systems for medium-long range distance measurement.
- In kinematics, TOF is the duration in which a projectile is traveling through the air. Given the initial velocity u of a particle launched from the ground, the downward (i.e. gravitational) acceleration a , and the projectile's angle of projection θ (measured relative to the horizontal), then a simple rearrangement of the SUVAT equation

$$s = vt - \frac{1}{2}at^2 \quad (2.3)$$

results in this equation

$$t = \frac{2v\sin\theta}{a} \quad (2.4)$$

for the time of flight of a projectile.

2.4. Cherenkov Radiation

Cherenkov radiation (also spelled Cerenkov or Čerenkov) is electromagnetic radiation emitted when a charged particle (such as an electron) passes through an insulator at a constant speed greater than the speed of light in that medium. The charged particles polarize the molecules of that medium, which then turn back rapidly to their ground state, emitting radiation in the process. The characteristic blue glow of nuclear reactors is due to Cherenkov radiation. It is named after Russian scientist Pavel Alekseyevich Cherenkov, the 1958 Nobel Prize winner who was the first to characterise it rigorously [9].

While relativity holds that the speed of light *in a vacuum* is a universal constant (c), the speed at which light propagates in a material may be significantly less than c . For example, the speed of the propagation of light in water is only $0.75c$. Matter can be accelerated beyond this speed during nuclear reactions and in particle accelerators. Cherenkov radiation results when a charged particle, most commonly an electron, travels through a dielectric (electrically polarizable) medium with a speed greater than that at which light would otherwise propagate in the same medium. Moreover, the velocity that must be exceeded is the phase velocity of light rather than the group

velocity of light. The phase velocity can be altered dramatically by employing a periodic medium, and in that case one can even achieve Cherenkov radiation with *no* minimum particle velocity—a phenomenon known as the Smith-Purcell effect. In a more complex periodic medium, such as a photonic crystal, one can also obtain a variety of other anomalous Cherenkov effects, such as radiation in a backwards direction (whereas ordinary Cherenkov radiation forms an acute angle with the particle velocity).

As a charged particle travels, it disrupts the local electromagnetic field (EM) in its medium. Electrons in the atoms of the medium will be displaced, and the atoms become polarized by the passing EM field of a charged particle. Photons are emitted as an insulator's electrons restore themselves to equilibrium after the disruption has passed. (In a conductor, the EM disruption can be restored without emitting a photon.) In normal circumstances, these photons destructively interfere with each other and no radiation is detected. However, when a disruption which travels faster than light is propagating through the medium, the photons constructively interfere and intensify the observed radiation.

A common analogy is the sonic boom of a supersonic aircraft or bullet. The sound waves generated by the supersonic body propagate at the speed of sound itself; as such the waves travel slower than the speeding object and cannot propagate forward from the body. Instead they form a shock front. In a similar way, a charged particle can generate a photonic shock wave as it travels through an insulator.

In the figure, the particle (red arrow) travels in a medium with speed v_p such that $c/n < v_p < c$, where c is speed of light in vacuum, and n is the refractive index of the medium. (If the medium is water, the condition is $0.75c < v_p < c$, since $n = 1.33$ for water at 20 °C.)

We define the ratio between the speed of the particle and the speed of light as $\beta = v_p/c$. The emitted light waves (blue arrows) travel at speed $v_{em} = c/n$. The left corner of the triangle represents the location of the superluminal particle at some initial moment ($t=0$). The right corner of the triangle is the location of the particle at some later time t . In the given time t , the particle travels the distance.

$$x_p = v_p t = \beta ct \quad (2.5)$$

whereas the emitted electromagnetic waves are constricted to travel the distance

$$x_{em} = v_{em} t = \frac{c}{n} t \quad (2.6)$$

So:

$$\cos \theta = \frac{1}{n\beta} \quad (2.7)$$

Note that since this ratio is independent of time, one can take arbitrary times and achieve similar triangles. The angle stays the same, meaning that subsequent waves generated between the initial time $t=0$ and final time t will form similar triangles with coinciding below endpoints to the one shown.

CHAPTER 3

3. The LHC and the ATLAS Experiment

3.1. The Large Hadron Collider (LHC)

The **Large Hadron Collider (LHC)** is the world's largest[10] and highest-energy particle accelerator. It is expected that it will address some of the most fundamental questions of physics, advancing humanity's understanding of the deepest laws of nature.

The LHC lies in a tunnel 27 kilometres in circumference, as much as 175 metres beneath the Franco-Swiss border near Geneva, Switzerland. This synchrotron is designed to collide opposing particle beams of either protons at an energy of 7 teraelectronvolts (7 TeV) per particle, or lead nuclei at an energy of 574 TeV (92.0 μ J) per nucleus. The term hadron refers to particles composed of quarks.

The Large Hadron Collider was built by the European Organization for Nuclear Research (CERN) with the intention of testing various predictions of high-energy physics, including the existence of the hypothesized Higgs boson and of the large family of new particles predicted by supersymmetry. It is funded by and built in collaboration with over 10,000 scientists and engineers from over 100 countries as well as hundreds of universities and laboratories. On 10 September 2008, the proton beams were successfully circulated in the main ring of the LHC for the first time, but 9 days later operations were halted due to serious fault. On 20 November 2009 they were successfully circulated again, with the first proton–proton collisions being recorded 3 days later at the injection energy of 450 GeV per beam. After the 2009 winter shutdown, the LHC was restarted and the beam was ramped up to 3.5 TeV per beam, half its designed energy. On 30 March 2010, the first planned collisions took

place between two 3.5 TeV beams, which set a new world record for the highest-energy man-made particle collisions.

3.1.1. The LHC Purpose

Physicists hope that the LHC will help answer many of the most fundamental questions in physics: questions concerning the basic laws governing the interactions and forces among the elementary objects, the deep structure of space and time, especially regarding the intersection of quantum mechanics and general relativity, where current theories and knowledge are unclear or break down altogether. These issues include, at least:

- Is the Higgs mechanism for generating elementary particle masses via electroweak symmetry breaking indeed realised in nature? It is anticipated that the collider will either demonstrate or rule out the existence of the elusive Higgs boson(s), completing (or refuting) the Standard Model .
- Is supersymmetry, an extension of the Standard Model and Poincaré symmetry, realised in nature, implying that all known particles have supersymmetric partners?
- Are there extra dimensions, as predicted by various models inspired by string theory, and can we detect them?
- What is the nature of the Dark Matter which appears to account for 23% of the energy density of the Universe?

Other questions are:

- Are electromagnetism, the strong nuclear force and the weak nuclear force just different manifestations of a single unified force, as predicted by various Grand Unification Theories?
- Why is gravity so many orders of magnitude weaker than the other three fundamental forces? See also Hierarchy problem.

- Are there additional sources of quark flavour mixing, beyond those already predicted within the Standard Model?
- Why are there apparent violations of the symmetry between matter and antimatter? See also CP violation.
- What was the nature of the quark-gluon plasma in the early universe? This will be investigated by heavy ion collisions in ALICE.

3.1.2. The design of the LHC

The LHC is the world's largest and highest-energy particle accelerator. The collider is contained in a circular tunnel, with a circumference of 27 kilometres (17 mi), at a depth ranging from 50 to 175 metres (160 to 574 ft) underground.

The 3.8-metre (12 ft) wide concrete-lined tunnel, constructed between 1983 and 1988, was formerly used to house the Large Electron–Positron Collider. It crosses the border between Switzerland and France at four points, with most of it in France. Surface buildings hold ancillary equipment such as compressors, ventilation equipment, control electronics and refrigeration plants.

The collider tunnel contains two adjacent parallel beam pipes that intersect at four points, each containing a proton beam, which travel in opposite directions around the ring. Some 1,232 dipole magnets keep the beams on their circular path, while an additional 392 quadrupole magnets are used to keep the beams focused, in order to maximize the chances of interaction between the particles in the four intersection points, where the two beams will cross. In total, over 1,600 superconducting magnets are installed, with most weighing over 27 tonnes. Approximately 96 tonnes of liquid helium is needed to keep the magnets at their operating temperature of 1.9 K ($-271.25\text{ }^{\circ}\text{C}$), making the LHC the largest cryogenic facility in the world at liquid helium temperature.

Once or twice a day, as the protons are accelerated from 450 GeV to 7 TeV, the field of the superconducting dipole magnets will be increased from 0.54 to 8.3 teslas (T). The protons will each have an energy of 7 TeV, giving a total collision energy of 14 TeV. At this energy the protons have a Lorentz factor of about 7,500 and move at

about 0.999999991 c , or about 3 metres per second slower than the speed of light (c). It will take less than 90 microseconds (μs) for a proton to travel once around the main ring – a speed of about 11,000 revolutions per second. Rather than continuous beams, the protons will be bunched together, into 2,808 bunches, so that interactions between the two beams will take place at discrete intervals never shorter than 25 nanoseconds (ns) apart. However it will be operated with fewer bunches when it is first commissioned, giving it a bunch crossing interval of 75 ns. The design luminosity of the LHC is $10^{34} \text{ cm}^{-2}\text{s}^{-1}$, providing a bunch collision rate of 40 MHz.

Prior to being injected into the main accelerator, the particles are prepared by a series of systems that successively increase their energy. The first system is the linear particle accelerator LINAC 2 generating 50-MeV protons, which feeds the Proton Synchrotron Booster (PSB). There the protons are accelerated to 1.4 GeV and injected into the Proton Synchrotron (PS), where they are accelerated to 26 GeV. Finally the Super Proton Synchrotron (SPS) is used to further increase their energy to 450 GeV before they are at last injected (over a period of 20 minutes) into the main ring. Here the proton bunches are accumulated, accelerated (over a period of 20 minutes) to their peak 7-TeV energy, and finally circulated for 10 to 24 hours while collisions occur at the four intersection points.

The LHC physics program is mainly based on proton–proton collisions. However, shorter running periods, typically one month per year, with heavy-ion collisions are included in the program. While lighter ions are considered as well, the baseline scheme deals with lead ions (see A Large Ion Collider Experiment). The lead ions will be first accelerated by the linear accelerator LINAC 3, and the Low-Energy Ion Ring (LEIR) will be used as an ion storage and cooler unit.

The ions will then be further accelerated by the PS and SPS before being injected into LHC ring, where they will reach an energy of 2.76 TeV per nucleon (or 575 TeV per ion), higher than the energies reached by the Relativistic Heavy Ion Collider. The aim of the heavy-ion program is to investigate quark–gluon plasma, which existed in the early universe.

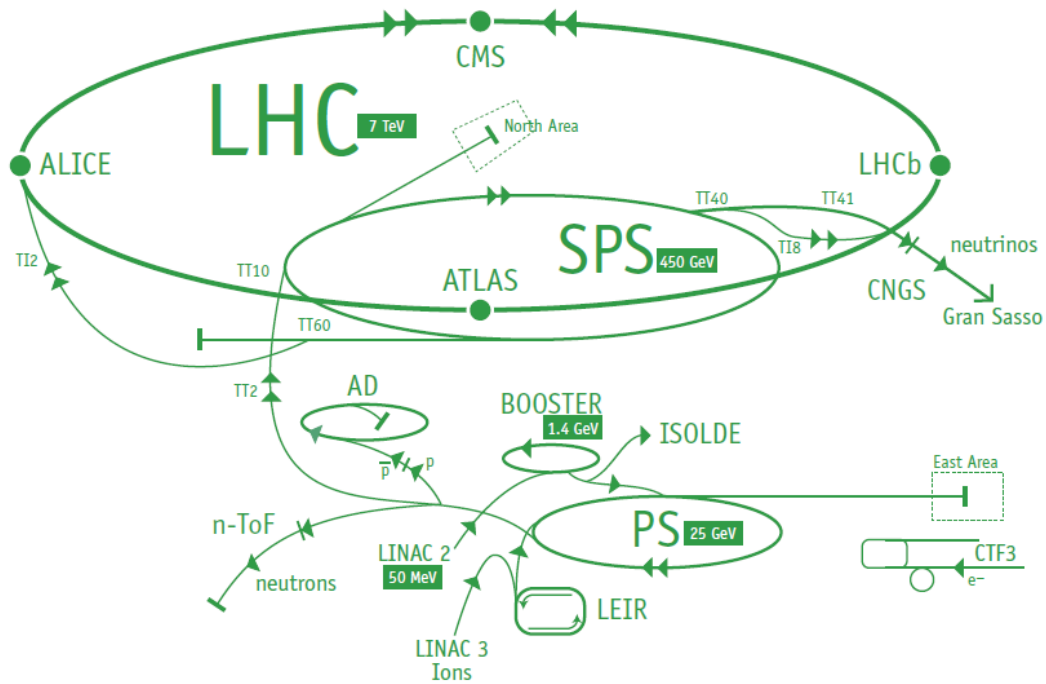


Figure 3.1. Overview of the LHC. Source [11]

3.1.3. The LHC experiments

The six experiments at the LHC are all run by international collaborations, bringing together scientists from institutes all over the world. Each experiment is distinct, characterised by its unique particle detector.

The two large experiments, ATLAS and CMS, are based on general-purpose detectors to analyse the myriad of particles produced by the collisions in the accelerator. They are designed to investigate the largest range of physics possible. Having two independently designed detectors is vital for cross-confirmation of any new discoveries made.

Two medium-size experiments, ALICE and LHCb, have specialised detectors for analysing the LHC collisions in relation to specific phenomena.

Two experiments, TOTEM and LHCf, are much smaller in size. The ATLAS, CMS, ALICE and LHCb detectors are installed in four huge underground caverns located around the ring of the LHC. The detectors used by the TOTEM experiment are positioned near the CMS detector, whereas those used by LHCf are near the ATLAS detector.

3.1.3.1. ALICE

ALICE is the acronym for A Large Ion Collider Experiment, one of the largest experiments in the world devoted to research in the physics of matter at an infinitely small scale. Hosted at CERN, the European Laboratory for Nuclear Research, this project involves an international collaboration of more than 1000 physicists, engineers and technicians, including around 200 graduate students, from 116 physics institutes in 33 countries across the world (as of November 2010). The ALICE Experiment is going in search of answers to fundamental questions, using the extraordinary tools provided by the LHC: What happens to matter when it is heated to 100,000 times the temperature at the centre of the Sun? Why do protons and neutrons weigh 100 times more than the quarks they are made of? Can the quarks inside the protons and neutrons be freed?

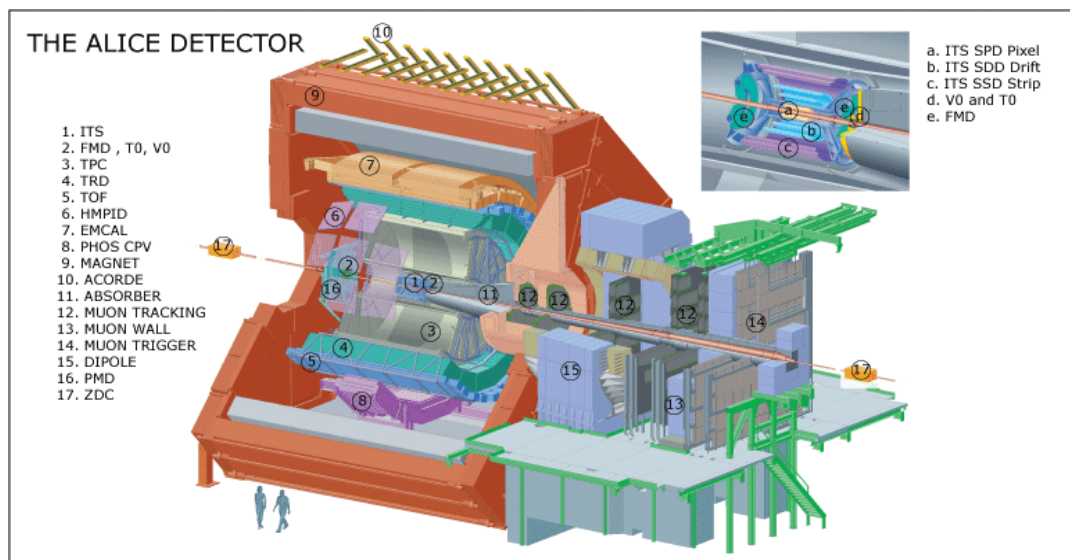


Figure 3.2. Overview of the ALICE. Source [12]

ALICE detector

Size: 26 m long, 16 m high, 16 m wide

Weight: 10 000 tonnes

Design: central barrel plus single arm forward muon spectrometer

Location: St Genis-Pouilly, France.

3.1.3.2. ATLAS

The ATLAS detector is described in detail in Section 3.2.

3.1.3.3. CMS

The CMS (Compact Muon Solenoid) experiment uses a general-purpose detector to investigate a wide range of physics, including the search for the Higgs boson, extra dimensions, and particles that could make up dark matter. Although it has the same scientific goals as the ATLAS experiment, it uses different technical solutions and design of its detector magnet system to achieve these.

The CMS detector [13] is built around a huge solenoid magnet. This takes the form of a cylindrical coil of superconducting cable that generates a magnetic field of 4 teslas, about 100 000 times that of the Earth. The magnetic field is confined by a steel 'yoke' that forms the bulk of the detector's weight of 12 500 tonnes. An unusual feature of the CMS detector is that instead of being built in-situ underground, like the other giant detectors of the LHC experiments, it was constructed on the surface, before being lowered underground in 15 sections and reassembled.

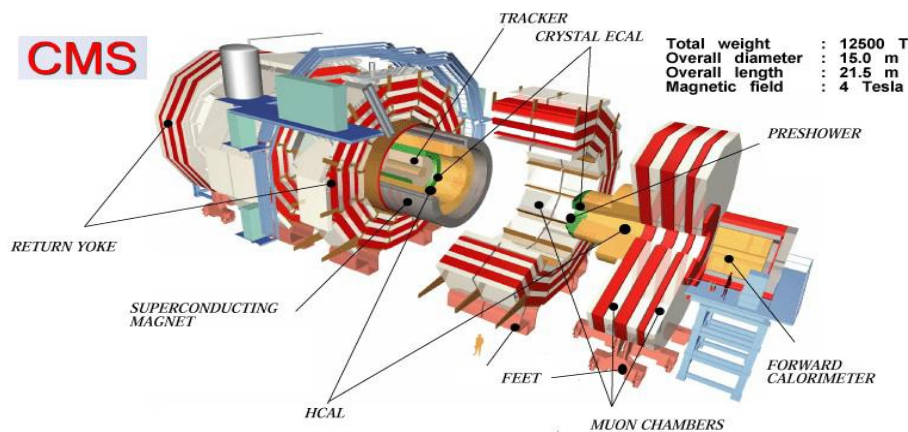


Figure 3.3. Overview of the CMS. Source [13]

More than 3600 scientists collaborate in CMS, coming from 183 institutes in 38 countries (June 2008).

3.1.3.4. LHCb

The LHCb (Large Hadron Collider beauty) experiment will help us to understand why we live in a Universe that appears to be composed almost entirely of matter, but no antimatter.

It specialises in investigating the slight differences between matter and antimatter by studying a type of particle called the 'beauty quark', or 'b quark'. Instead of surrounding the entire collision point with an enclosed detector, the LHCb experiment uses a series of sub-detectors to detect mainly forward particles. The first sub-detector is mounted close to the collision point, while the next ones stand one behind the other, over a length of 20 m.

An abundance of different types of quark will be created by the LHC before they decay quickly into other forms. To catch the b-quarks, LHCb has developed sophisticated movable tracking detectors close to the path of the beams circling in the LHC. The LHCb collaboration has 700 scientists from 57 institutes in 15 countries (2008).

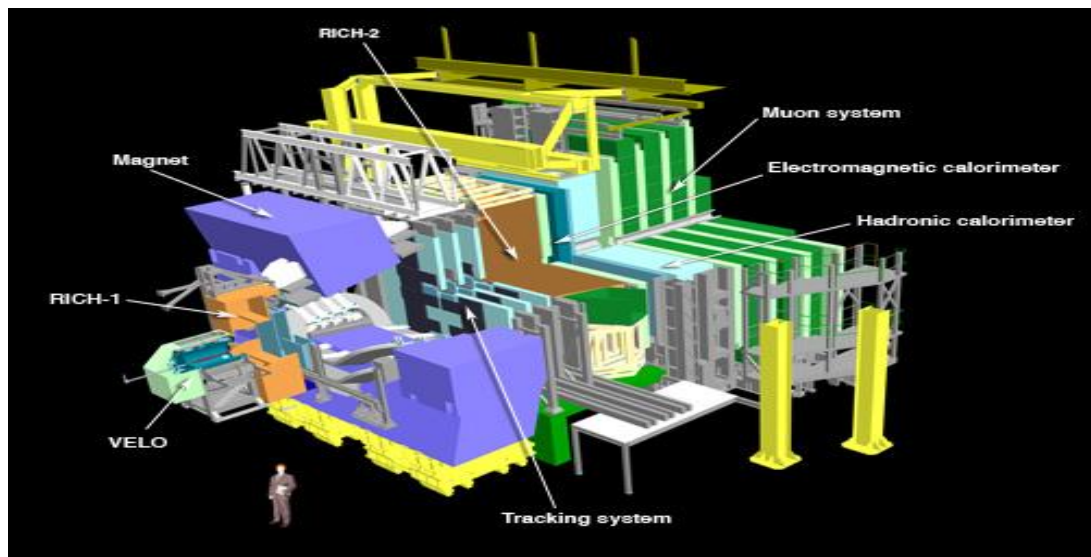


Figure 3.4. Overview of the LHCb. Source [14]

LHCb detector:

Size: 21m long, 10m high and 13m wide

Weight: 5600 tonnes

Design: forward spectrometer with planar detectors

Location: Ferney-Voltaire, France.

3.1.3.5. TOTEM

The TOTEM(TOTAL Elastic and diffractive cross section Measurement) experiment studies forward particles to focus on physics that is not accessible to the general-purpose experiments. Among a range of studies, it will measure, in effect, the size of the proton and also monitor accurately the LHC's luminosity.

To do this TOTEM must be able to detect particles produced very close to the LHC beams. It will include detectors housed in specially designed vacuum chambers called 'Roman pots', which are connected to the beam pipes in the LHC. Eight Roman pots will be placed in pairs at four locations near the collision point of the CMS experiment.

Although the two experiments are scientifically independent, TOTEM will complement the results obtained by the CMS detector and by the other LHC experiments overall. The TOTEM experiment involves 58 scientists from 10 institutes in 8 countries (2010).

TOTEM detector:

Size: 440 m long, 5 m high and 5 m wide

Weight: 20 tonnes

Design: Roman pot and GEM detectors and cathode strip chambers

Location: Cessy, France (near CMS)

3.1.3.6. LHCf

The LHCf (Large Hadron Collider forward) experiment uses forward particles created inside the LHC as a source to simulate cosmic rays in laboratory conditions.

Cosmic rays are naturally occurring charged particles from outer space that constantly bombard the Earth's atmosphere. They collide with nuclei in the upper atmosphere, leading to a cascade of particles that reaches ground level.

Studying how collisions inside the LHC cause similar cascades of particles will help scientists to interpret and calibrate large-scale cosmic-ray experiments that can cover thousands of kilometres. The LHCf experiment involves 22 scientists from 10 institutes in 4 countries (September 2006).

LHCf detector

Size: two detectors, each measures 30 cm long, 80 cm high, 10 cm wide

Weight: 40 kg each

Location: Meyrin, Switzerland (near ATLAS)

3.2.ATLAS

ATLAS (A Toroidal LHC ApparatuS) [15] is one of the six particle detector experiments (ALICE, ATLAS, CMS, TOTEM, LHCb, and LHCf) constructed at the Large Hadron Collider (LHC), a new particle accelerator at the European Organization for Nuclear Research (CERN) in Switzerland. ATLAS is 44 metres long and 25 metres in diameter, weighing about 7,000 tonnes. The project is led by Fabiola Gianotti and involves roughly 3,000 scientists and engineers at 174 institutions in 38 countries. The construction was originally scheduled to be completed in June 2007, but was ready and detected its first beam events on 10 September 2008. The experiment is designed to observe phenomena that involve highly massive particles which were not observable using earlier lower-energy accelerators and might shed light on new theories of particle physics beyond the Standard Model.

The ATLAS collaboration, the group of physicists building the detector, was formed in 1992 when the proposed EAGLE (Experiment for Accurate Gamma, Lepton and Energy Measurements) and ASCOT (Apparatus with Super COnducting Toroids) collaborations merged their efforts into building a single, general-purpose particle detector for the Large Hadron Collider. The design was a combination of those two previous designs, as well as the detector research and development that had been done for the Superconducting Supercollider. The ATLAS experiment was proposed in its current form in 1994, and officially funded by the CERN member countries beginning in 1995. Additional countries, universities, and laboratories joined in subsequent years, and further institutions and physicists continue to join the collaboration even today. The work of construction began at individual institutions, with detector components shipped to CERN and assembled in the ATLAS experimental pit beginning in 2003.

ATLAS is designed as a general-purpose detector, Figure 3.5. When the proton beams produced by the Large Hadron Collider interact in the center of the detector, a variety of different particles with a broad range of energies may be produced. Rather than focusing on a particular physical process, ATLAS is designed to measure the broadest possible range of signals. This is intended to ensure that, whatever form any new physical processes or particles might take, ATLAS will be able to detect them and measure their properties. Experiments at earlier colliders, such as the Tevatron and Large Electron-Positron Collider, were designed based on a similar philosophy. However, the unique challenges of the Large Hadron Collider—its unprecedented energy and extremely high rate of collisions—require ATLAS to be larger and more complex than any detector ever built.

3.2.1. The ATLAS experiment

Being a general purpose detector, the list of physics performance goals is, of course, extensive. However, some measurements stand out as being of particular importance. Discovering the Higgs boson is such a measurement. As discussed previously, the Higgs can, if it exists, have any mass in the 102GeV range, and it must be ensured in the detector design, that discovery is possible regardless of its mass. Since the branching ratio of the Higgs into its various decay channels differs significantly as a

function of the Higgs mass, this implies that the experiment must be designed to have sufficient sensitivity in a large number of different decay channels. Another physics goal of vital importance is the possible SUSY discovery. Similar to the Higgs boson case, the masses of the SUSY particles are largely unconstrained, and possible discovery depends on the performance of a number of sub-detector systems and their combined performance to reconstruct missing transverse energy $=E_T$. The expected cross-sections of the Higgs and SUSY processes are exceedingly small even at LHC energies:

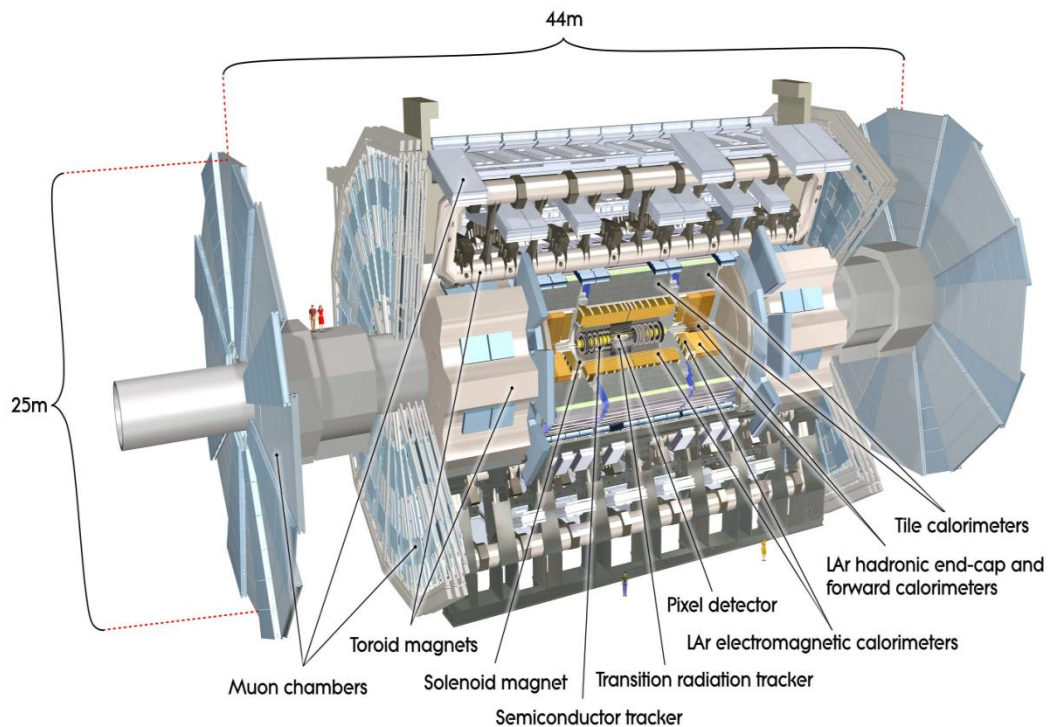


Figure 3.5. Overview of the ATLAS detector, Source [15]

About 1 event in a billion This is the reason to aim for the high interaction rate (40 MHz). Obviously the high interaction rate and the resulting large track multiplicities complicate the detector design. In order to be able to perform in the environment provided by the LHC machine, the physics performance goals can be translated into a set of detector requirements on which the ATLAS experiment has been designed:

- To cope with the interaction rate and the particle multiplicity, the electronics of all sub-detectors must be fast and radiation hard. Also, the detector granularity must be

sufficiently fine so that the interesting events can be reconstructed despite the many overlapping events.

- For overall event reconstruction, and in particular to reconstruct secondary vertexes from b or τ decays, the charged particle momentum must be measured with a high resolution and efficiency:

$$\sigma_{P_T}/P_T = 0.05\% \cdot P_T \oplus 1\%$$

- Large acceptance in pseudorapidity and full azimuthal coverage is essential.
- To identify and precisely measure the energy of electrons and photons the electromagnetic calorimeter must perform well:

$$\sigma_{E/E} = 10\% \sqrt{E} \oplus 0.7\%$$

In addition, the hadronic calorimeter measures the energies of hadrons and jets:

$$\sigma_{E/E} = 50\% \sqrt{E} \oplus 3\% \text{ (barrel) and}$$

$$\sigma_{E/E} = 100\% \sqrt{E} \oplus 10\% \text{ (end-cap).}$$

- Muons must be accurately identified and measured:

$$\sigma_{P_T/P_T} = 10\% \text{ at } P_T = 1 \text{ TeV.}$$

- Events must be sorted on a short timescale so that uninteresting events can be rejected, thereby ensuring that the maximal output event rate is below the hardware limitation of about 200 Hz.

How these requirements are met by the ATLAS experiment is briefly discussed in the following.

3.2.1.1. The Inner Detector

The tracking of charged particles is performed by the Inner Detector. This detector is built utilizing a typical layered structure, consisting of three sub-detectors based on different detector technologies to best cope with the requirements. Each sub-detector

consists of a barrel part and two end-caps as shown in Figure 3.6. The resolutions quoted below represent the values of [15] which is the most recent assessment.

3.2.1.1.1. The Pixel Detector

Closest to the interaction point is the very radiation hard and finely segmented Pixel Detector (Pixel), whose pixels are as small as $50 \times 400 \mu\text{m}^2$. The sensitive detectors of the Pixel barrel are placed on concentric cylinders around the beam-line, whereas the end-caps consist of disks placed perpendicular to the beam axis, extending to $|z| \approx 50 \text{ cm}$, as indicated in Figure 3.7.

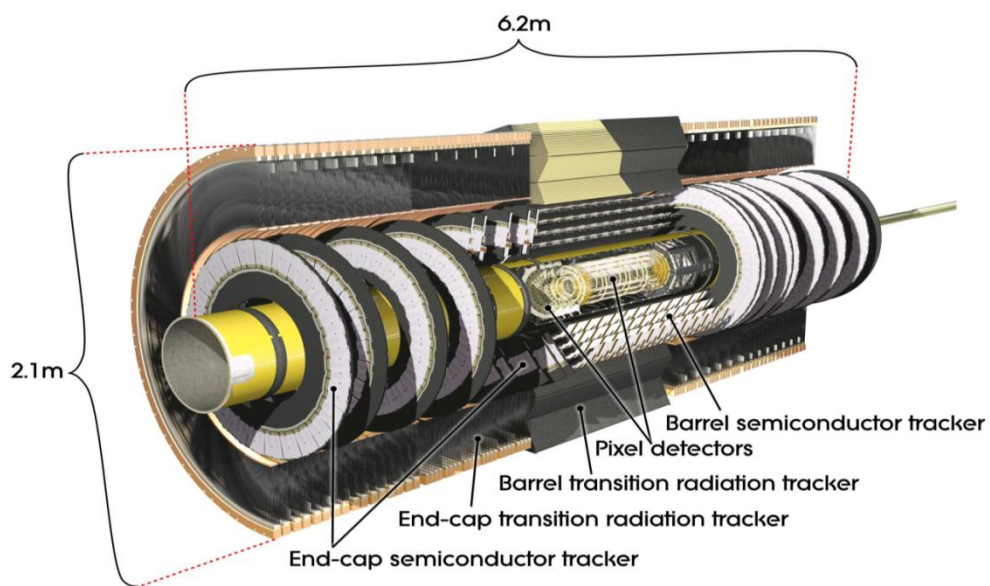


Figure 3.6. The structure of the Inner Detector. Source [15]

Altogether the pixel detector counts 80.4 million read-out channels, providing three measurements for each track. In the barrel the expected intrinsic accuracy is $10 \mu\text{m}$ in $r\phi$ and $115 \mu\text{m}$ in the z plane whereas the corresponding values for the end-caps are $10 \mu\text{m}$ in $r\phi$ and $115 \mu\text{m}$ in the r direction. The innermost layer of the Pixel detector is placed merely 5.1 cm from the nominal beam position whereas layers two and three are located at 8.9 cm and 12.3 cm respectively. For this reason, the Pixel detector is subject to a significant radiation dose. Despite significant efforts to limit the effects caused by this, the harsh hadron environment in which the Pixel detector

operates, causes the detector to degrade over time. It is expected that the detector will be replaced at a future detector upgrade.

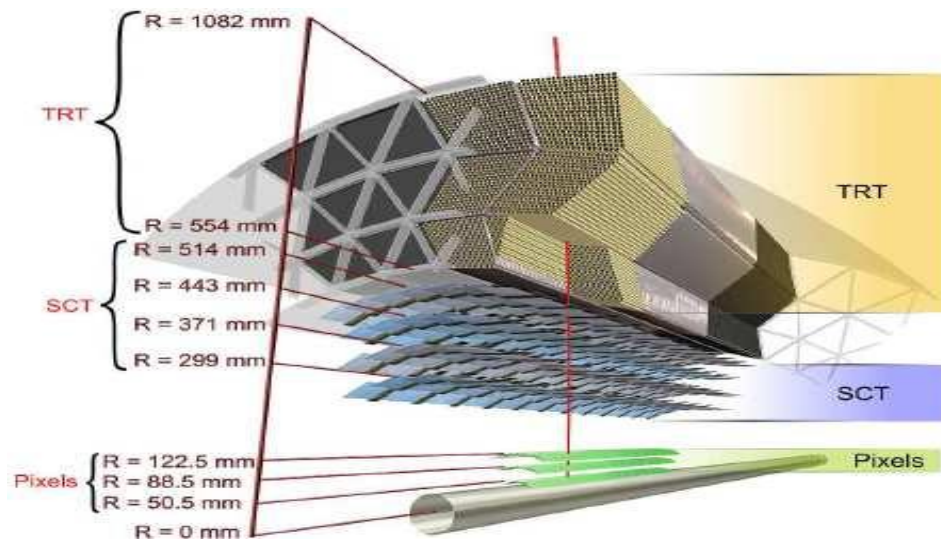


Figure 3.7. The structure of the Inner Detector barrel. Source [15]

3.2.1.1.2. The SCT

The next sub-detector met by a traversing particle consists of the four double-sided silicon layers of the SemiConductor Tracker (SCT) - a silicon micro-strip detector with a read-out pitch of $80 \mu\text{m}$. Due to a small stereo angle between the read-out strips, the SCT provides four space-points for each penetrating track. Arranged in a setup similar to the Pixel detector (see Figure 3.7), the SCT barrel yields a binary resolution of $17 \mu\text{m}$ in $r\phi$ and $580 \mu\text{m}$ in z . In the end-caps the same $r\phi$ resolution is achieved whereas the resolution in r is $580 \mu\text{m}$. Altogether, the SCT has 6.3 million read-out channels and occupies the region: $30 \text{ cm} < r < 52 \text{ cm}$ and $|z| < 2.8 \text{ m}$.

3.2.1.1.3. The TRT

The TRT is described in detail in Chapter 4.

3.2.1.2. Calorimeters

The ATLAS calorimetry consists of an inner electromagnetic calorimeter supplemented by a dense hadronic calorimeter as depicted in Figure 3.8 (top). The electromagnetic calorimeter is built using an accordion structure of lead plates

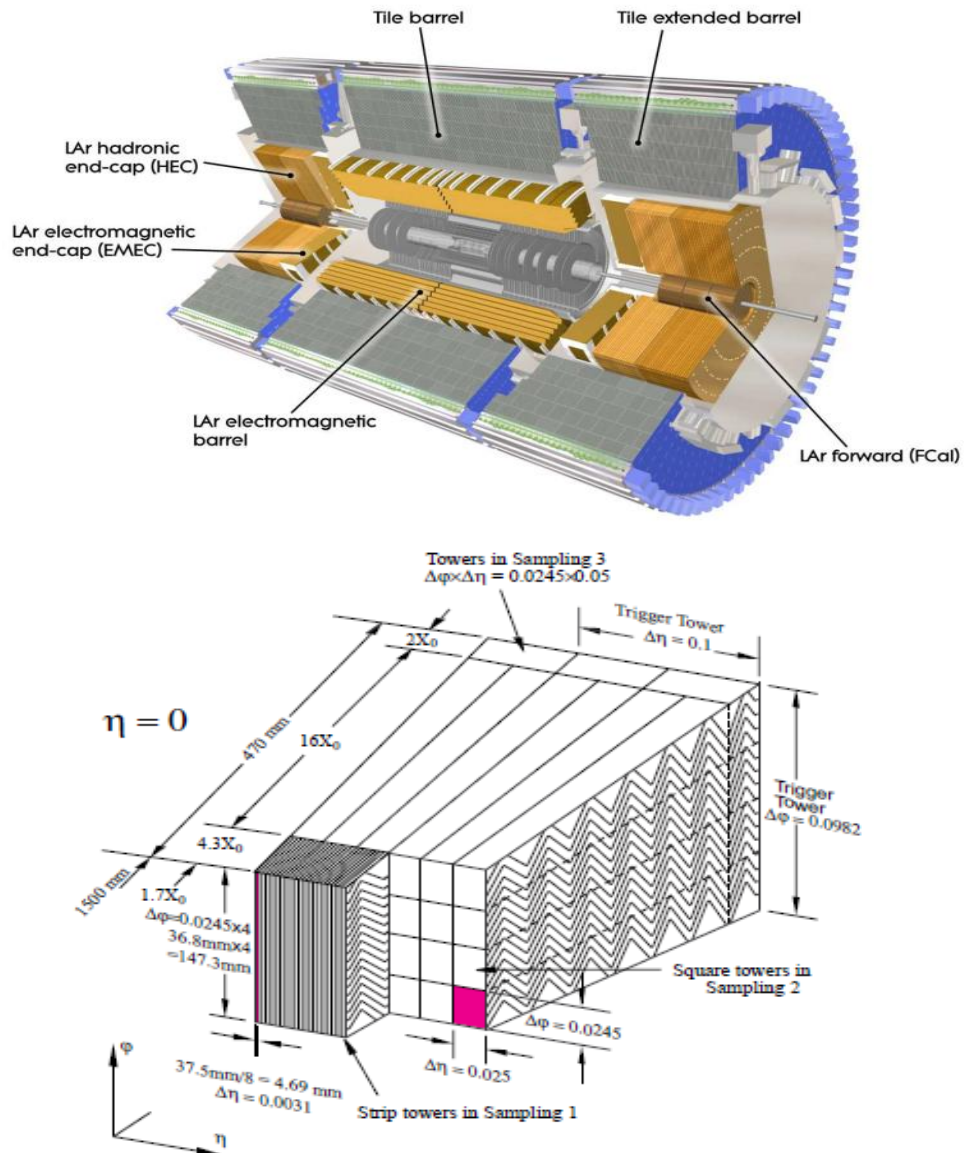


Figure 3.8. top: Overview of the calorimeter systems. Bottom: The structure of the LAr calorimeter. Source [15]

interleaved with liquid argon (LAr) and functions basically as a drift-chamber due to a strong electric field. This design has the advantages of complete ϕ symmetry without azimuthal cracks, and moreover the active LAr can be replaced during detector operation, hereby minimizing effects of radiation damage. The detector covers the region up to $r = 2.25$ m corresponding to >22 (>24) radiation lengths in the barrel (end-caps). The granularity shown in figure 2.1.4(right) corresponds to that of the central barrel part ($\eta = 0$). Along η , the cell size varies significantly as determined by an optimization of the energy resolution. The very fine segmented innermost sampling is designed for e/p separation, whereas most energy is deposited in the square sampling towers of the second sampling. For triggering purposes, 4 by 4 cells are combined into towers with a single output. The hadronic calorimeter covers the region up to $r = 4.25$ m and consists of a barrel part, two extended barrels, two end-caps and two forward calorimeters. In order to reduce the effects of the radiation the latter two sub-detectors, which are subject to the largest track multiplicity, are based on LAr. The first two sub-systems are sampling calorimeters using steel absorbers and scintillating tiles of plastic. The readout proceeds via wavelength shifting fibers to photomultiplier tubes placed on the outer rim of the calorimeter. The total thickness of the tile calorimeter is 9.7 radiation lengths at $\eta = 0$. As for the electromagnetic calorimeter, the cell sizes differ significantly in η and it serves little purpose to repeat them here. Instead, the reader is referred to [15].

3.2.1.3. The Muon System

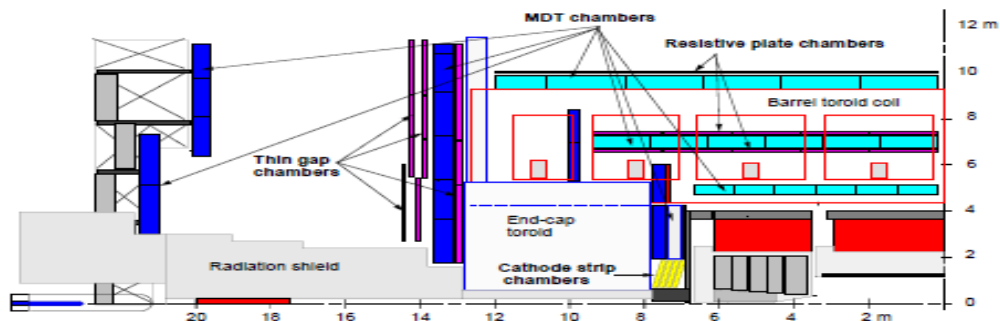


Figure 3.9. Overview of the Muon System. Source [15]

Due to the thickness of the calorimeters, the punch-through probability of hadrons into the Muon

System is low, so that hits in this system can reliably be assumed to be caused by muons. However, the purpose of the Muon System is not only to identify muons, but also to provide precision measurements of muon momenta and to be used for triggering. The combination of these requirements have led to the complex design of the muon system sketched. The Muon System consists of a barrel region and two end-cap regions located partially within the toroids magnets (see Figure 3.9). In the barrel, sensitive monitoring drift tubes (MDT) are placed on three cylindrical layers whereas the end-cap regions uses vertical concentric structures. The tubes, which are built of aluminum, have a diameter of 3 cm and are filled with a mixture of Argon (93%) and CO₂ (7%) operating under a pressure of 3 bar. Centrally in the tubes, an anode wire composed of W-Re collects the electrons freed by a passing muon. The spatial resolution which can be achieved by this design is about 80 μ m per measurement.

In the regions of larger pseudo-rapidities, the requirements of segmentation and radiation hardness are more severe, and here measurements are performed by the cathode strip chambers (CSC). This multi-wire proportional chamber uses a $ArCO_2CF_4$ (30:50:20) gas-mixture [15], which provide a single hit resolution ~ 60 μ m.

For triggering purposes, the MDTs and CSCs are not useful due to the long drift times involved (up to 700 ns) and therefore two separate sub-systems have been built: Resistive plate chambers (RPC) in the barrel region and thin gas chambers (TGC). The main reason to base the trigger chamber on different technologies is the difference in occupancy between the barrel and the end-cap. Both sub-detectors are based on small gas volumes and provide drift-times of typically 10 ns.

As opposed to other sub-systems, the space limitations faced by the Muon System are not severe, and thus the advantages of long lever arms can be afforded. For example, are the MDTs of the barrel layers placed at radii of 4.93 m, 7.12 m and 9.48 m respectively.

3.2.1.4. The magnet system

For the Inner Detector, a magnetic field of approximately 2 T is provided by the central solenoid (CS) [15], situated at $1.22 \text{ m} < r < 1.31 \text{ m}$. In order to prevent heating problems induced on the surrounding subdetectors, the central solenoid is based on a superconducting mixture of NbTi, Cu and Al cooled by liquid helium. The fact that the magnet is placed in front of the calorimeters allows its size to be small, but also implies that electromagnetic showers tend to start in the magnet rather than in the calorimeter. In order to diminish this effect and prevent unnecessary degrading of the calorimeter performance, the magnet is constructed using a minimum of material. In addition, the magnet is located inside a vacuum vessel shared by the electromagnetic calorimeter hereby eliminating two vacuum walls.

Muons are bent by the barrel- and end-cap air-core toroids, which are based on the same superconducting alloy as the central solenoid. The huge toroid system encapsulates the experiment, except for parts of the muon layers. Needless to say, the fields provided vary significantly in the volume of the ATLAS experiment, peaking at approximately 4 T.

3.2.1.5. Triggering

The bunch crossing rate at the LHC is 40 MHz. At the design luminosity of $10^{34} \text{ cm}^{-2} \text{ s}^{-1}$, the expected interaction rate is about 1GHz. The trigger system is designed to reduce this rate by a factor 107, down to the 100 Hz rate acceptable by the data-acquisition (DAQ) system for permanent storage. The interesting physics processes must clearly be accepted with high efficiency, while the overwhelming minimum bias events (events with many low pT hadrons resulting from fusion processes of gluons or quarks with a small energy transfer) must be very efficiently rejected. The trigger/DAQ system is schematized in Fig. 2.7. The level-1 (LVL1) trigger makes an initial selection based on reduced-granularity information from the muon trigger chambers and the calorimeters. The LVL1 trigger latency (the time taken to form and deliver the LVL1 trigger decision) is less than $2.5 \mu\text{s}$ (during this time the data from all the sub-detectors are stored in pipeline memories) and reduces the event rate to about 75 kHz, a value that is acceptable by all the ATLAS front-end

systems. The LVL1 trigger searches for several interesting signatures. The RPCs and TGCs trigger chambers are used to identify high- p_T muons,

while high- p_T electrons and photons, jets and τ -leptons decaying into hadrons are searched for in reduced granularity regions (towers) in the calorimeter. Information from large missing and total transverse energy, calculated by summing over trigger towers in the calorimeter, is also used at the LVL1 trigger. Events accepted by the LVL1 trigger are read-out from the front-end electronics systems of the detector into readout drivers (RODs) and then transferred into readout buffers (ROBs). Intermediate buffers, called derandomizers, average out the high instantaneous data rate at the output of the pipeline memories to match the available input bandwidth of the RODs. The data for the bunch crossing selected by the LVL1 trigger are held into the ROBs during the LVL2 trigger latency (expected in the range 1-10ms). The trigger rate is reduced by LVL2 to about 1 kHz. The LVL2 trigger uses 'region-of-interest' (RoI) information provided by the LVL1 trigger, such as the position (η and ϕ), the p_T of candidate objects and energy sums, and uses information from all the sub-detectors. In case of a muon trigger,

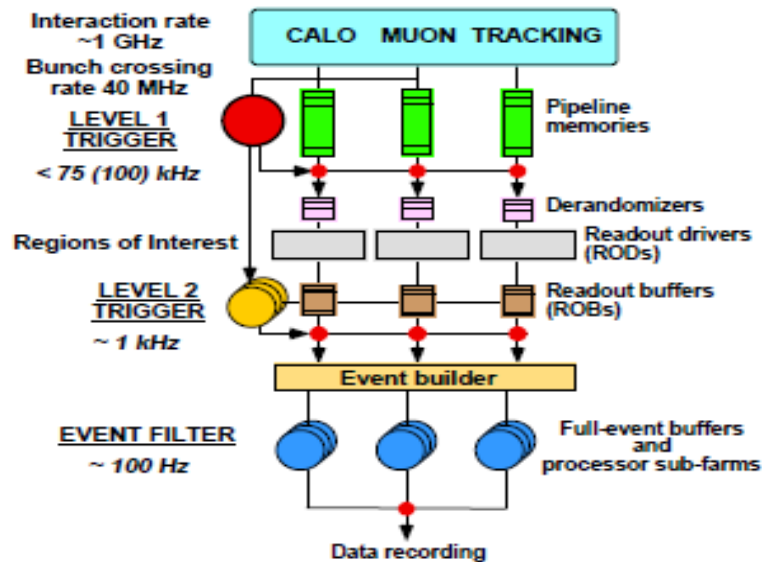


Figure 3.10. Overview of the ATLAS triggering scheme. Source [16]

the additional rejection power due to the LVL2 comes from a sharpening of the pT threshold, using also information from the precision muon chambers and the inner detector, and from the requirement for the muon to be isolated, using calorimeter information around a narrow region around the muon candidate. For isolated electrons, rejection power at the LVL2 comes from using the full granularity calorimeter information, from the requirement of a matching high- pT charged track in the inner detector, and from the use of transition-radiation information of the TRT. For photons, additional rejection power is limited by the relatively high probability for photon conversion in the inner detector material, so the use of the inner detector is not allowed. For the hadron/ τ trigger, a localised isolated hadronic calorimeter cluster with a matching high- pT inner detector track is required. If the event is accepted by LVL2, the data is transferred by the DAQ system to the Event Filter (EF), which constitutes the LVL3 trigger. The process of moving the data from the ROBs to the EF is called the event builder. The EF employs offline algorithms and methods, using up to date calibration and alignment information such as the magnetic field map. Most of the rejection power of the EF, that reduces the rate to 100 Hz, comes from the use of complex algorithms and criteria which, because of processing time limits, cannot be performed at LVL2, such as vertex and track fitting using bremsstrahlung recovery for electrons.

CHAPTER 4

4. The Transition Radiation Tracker

The Transition Radiation Tracker (TRT) [17] is a drift-tube system that, together with silicon-strip and pixel detectors at low radii, constitutes the tracking system of ATLAS, the Inner Detector¹. It is meant to provide robust tracking information with stand-alone pattern recognition capability in the LHC environment, to enhance the momentum resolution by providing track measurement points up to the solenoid radius and to provide a fast level-2 trigger. By integrating the transition-radiation signature, the TRT also provides stand-alone electron/pion separation (Fig. 4.1, top).

4.1. Detector Description

The TRT consists of a barrel part and two end-cap sides. The perspective view of the TRT layout is shown in Fig. 4.1, while the schematic view of the TRT detector in the R-z plane is shown in Fig. 4.2.

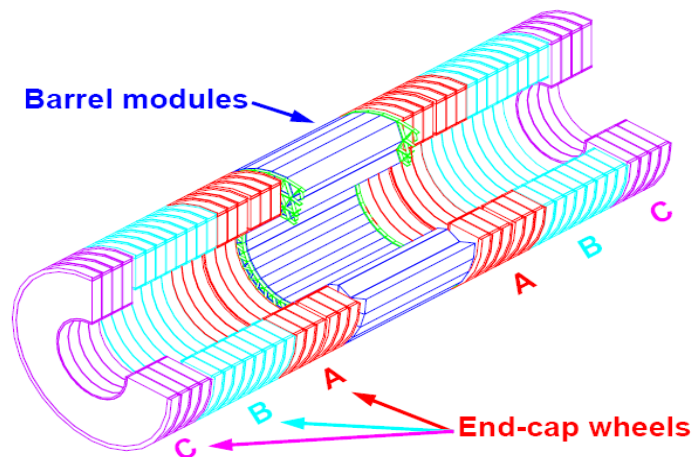


Figure 4.1. Schematic 3D-view of the TRT. Source [17]

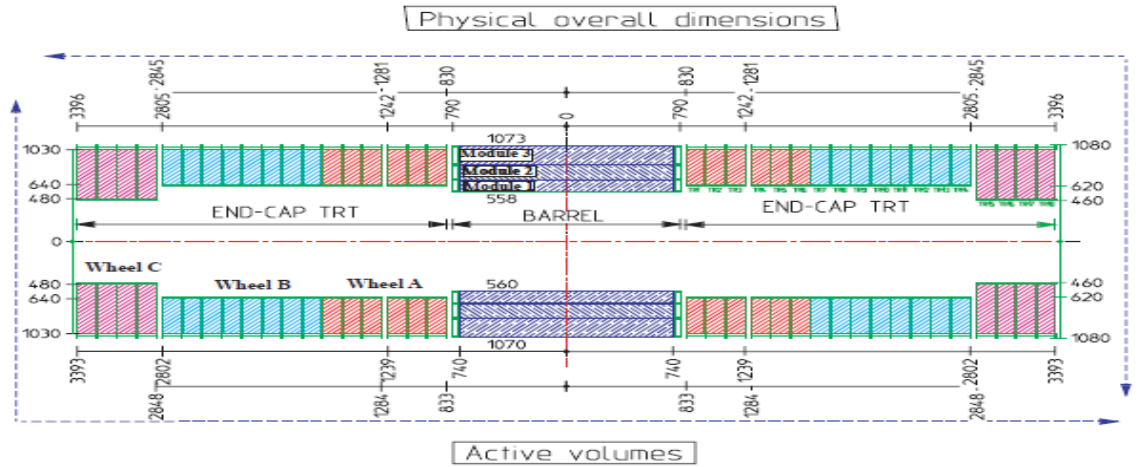


Figure 4.2. Schematic view of the TRT detector in the R-z plane. The main dimension of the detector are shown on the left (resp. right) hand side for the active detector volume (resp. the physical detector envelopes). Units are in mm. source [4]

The barrel part consists of three cylindrical rings, each containing 32 identical and independent modules. The three types of modules contain respectively 329 (type I modules, at the innermost radii), 520 (type II modules, at the middle radii) and 793 straws (type III modules, at the outermost radii). In the barrel, the straws are ± 70 cm long, placed axially with respect to the beam and are embedded in fiber radiator. In the end-caps the straws are shorter (between 39 cm and 55 cm) and are placed radially.

Each of the two end-caps consists of three sets of identical and independent wheels. In the wheels straws and radiator layers are alternated. In order of increasing distance from the interaction point they are: the type-A wheel (6 wheels with 12288 straws each), the type-B wheel (8 wheels with 6144 straws each) and the type-C wheels (4 wheels with 9216 straws each). The type-C wheels extend towards the beam pipe more than the other type of wheels, in order to maintain an approximately constant number of straws crossed by a track also at large η .

The detector modularity (both for barrel and end-caps) simplifies the assembly procedures and minimizes at every stage the number of straws affected by any failure

in the overall system. The engineering envelopes of the TRT modules are larger than the active modules, as can be seen, for example, in Fig. 3.2 in the barrel region between $z=740\text{mm}$ (edge of the active volume) and $z=790\text{mm}$ (edge of the engineering envelope). This accounts for the space needed to place cables, services, front-end electronics and mechanical support frames. In the barrel TRT the straw wires are electrically disconnected in the middle, in order to reduce the occupancy, and the signals are read out on either side of the modules. In the end-caps, on the other hand, the signals are read out just at the outer radius, minimizing in such a way the material at the inner radius.

4.2. Expected performance of the TRT

The TRT is designed to provide pattern recognition and level-2 trigger, momentum measurement and electron identification. The first three requirements are reached together with the precision pixel/SCT tracker, the fourth one jointly with the calorimeter.

- High- p_T isolated muons and electrons must be identified at level-2 with high efficiency guided by the relevant level-1 Region of Interest (RoI) defined in Section 2.6. The level-2 algorithm uses a very fast and robust histogramming technique; the algorithm scans all the relevant RoI and the number of hit straws corresponding to a given p_T bin are recorded as soon as the pattern of crossed straws changes. The histogram, shown in Fig. 3.3, contains therefore a very large number of bins and the signal from isolated electrons and muons can be seen above the fluctuations of the pile-up background.

- The TRT contributes to the momentum measurement by providing measurements of the track position in a large number of straws. A track will cross on average 35 straws, and a large fraction of them will give a hit (i.e. will yield a measured drift time within a two-standard-deviation window from the reconstructed

position of the track). The hit efficiency depends partially on η and largely on luminosity [21]. At low luminosity, for example, the hit efficiency is expected to be around 90%, providing therefore 32 measurements per track. In this case, the spatial resolution per straw is expected to be $170\ \mu\text{m}$ averaged over all straw layers.

- Electron identification in the TRT is achieved normally using the transition radiation

cluster-counting technique.

- A novel technique for particle identification in the TRT, namely the time-overthreshold, may improve electron identification at low energy and can provide, as well, some hadron identification. An example is given in Figure 4.3.

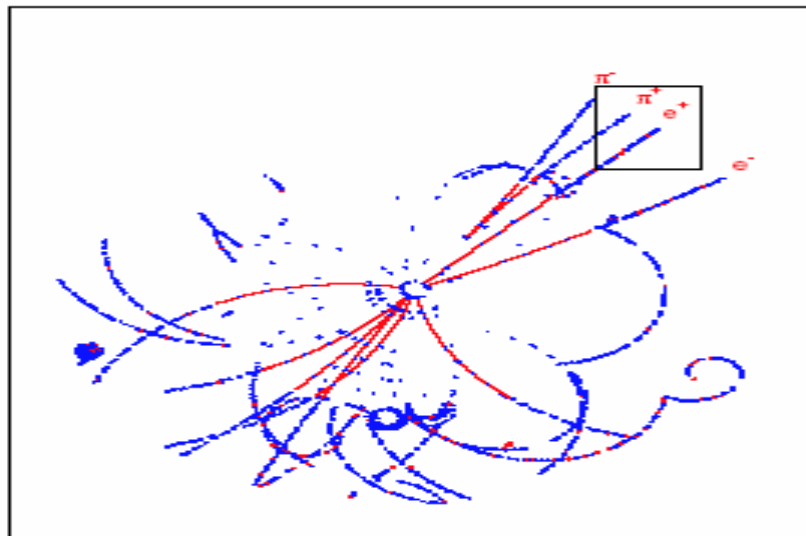


Figure 4.3. $B_d^0 \rightarrow j/\psi K_s^0$ simulated event display in the Inner Detector

4.3. The TRT straw drift-tube

The basic detecting element of the TRT is the straw drift-tube. A drift-tube is a gaseous detector which is used to measure the position of the track inside the tube. This measurement is performed by very accurately detecting the time that the electron clusters, released in the gas by the ionizing particle, take to drift to the anode wire.

The TRT straw tubes are 4mm in diameter and less than 150 cm in length. The maximum length is dictated by the overall detector dimensions and the maximum acceptable straw occupancy at the LHC. The 4mm radius, which gives a 42 ns maximum collection time of the signal, is a compromise between different requirements:

- the detector should respond as fast as possible to ionizing particles (this is crucial at the LHC, since the proton beams collide each 25 ns);
- the straw signal should be large enough to be detectable by the front-end electronics (reducing the diameter of the straws shortens the maximum collection time of the signal, but reduces as well the number of ionization clusters);
- the number of straws crossed by the track should be as large as possible, in order to maximize the number of measurements; this is important for particle identification and momentum measurement.

The TRT straw tube functions as an ionization chamber in the proportional regime, since the charge collected on the wire is proportional to the ionizing particle energy loss. The front-end electronics has been designed to provide a very accurate determination of the time of the leading edge of the signal above the 200 eV low-threshold discriminator level. It also detects very large energy depositions (above the 6 keV high-threshold discriminator level), which may be a consequence of a transition-radiation photon absorption, providing therefore the electron signature required of the TRT. The width of the low-threshold discriminator signal also provides partial information about the energy loss of a particle crossing the straw, enhancing therefore the particle identification capability of the TRT detector.

4.4. Gas composition

The gas mixture that has been chosen for the TRT is 70% Xe, 20% CF_4 , 10% CO_2 . The choice of Xenon as the main component of the gas mixture is dictated by the necessity to absorb very efficiently photons in the X-ray region. The drawback of this choice, apart from the cost, is the very slow positive ion tail (which needs to be removed by the front-end electronics) with respect to the choice of Argon gas for many detectors. The CF_4 is a molecular gas, which is used to make the gas as fast as possible, minimizing therefore the pile-up in time, which consists of overlapping signals from particles produced in interactions that occurred before or after the bunch crossing of interest. At the LHC, this is a crucial issue since the time between successive bunch crossing is just 25 ns. Since the Xe- CF_4 mixture is rather prone to high-voltage discharge, a small amount of CO_2 is added to stabilize the mixture. The

maximum charge-collection time is determined by the electron drift velocity, which in turn is a function of the electric field in the straw, and depends on the magnitude and the direction of the magnetic field. The dependence of the charge-collection time on the CF_4 concentration is shown in Fig. 4.4, for a ternary mixture containing 70% Xe, in a 2T magnetic field and for the nominal straw gain of $2.5 \cdot 10^4$. The remainder of the gas is CO_2 .

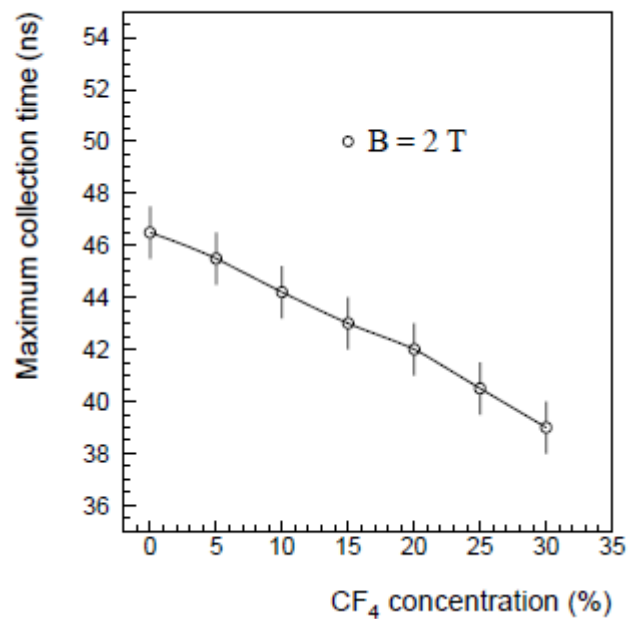


Figure 4.4. Total predicted charge-collection time in a magnetic field of 2T as a function of the CF_4 concentration for straws with a gas mixture containing 70% Xe and at their nominal gas gain of $2.5 \cdot 10^4$. The remainder of the gas is CO_2 . Source [4]

4.5. Barrel Modules

A barrel module, as illustrated in Fig. 4.5, is housed in a carbon-fiber shell. The carbon-fiber material has been chosen for his stiffness, necessary to keep the module straight, and for the high thermal conductivity required to carry out the heat produced in the straws via cooling tubes placed in two diagonal corners. The shell supports the radiators and the alignment planes, necessary to align the straws. The alignment planes are $100 \mu\text{m}$ thick Kapton sheets with a pattern of 4.3mm diameter holes and are positioned every 25 cm along the module within the shell. This configuration keeps the straws straight over the full length of the barrel module. The alignment

planes have a set of tabs on each side that pass through small holes in the shell. Holes punched in these tabs allow the Kapton sheets to be aligned on an external frame, and then to be glued to the shell after alignment.

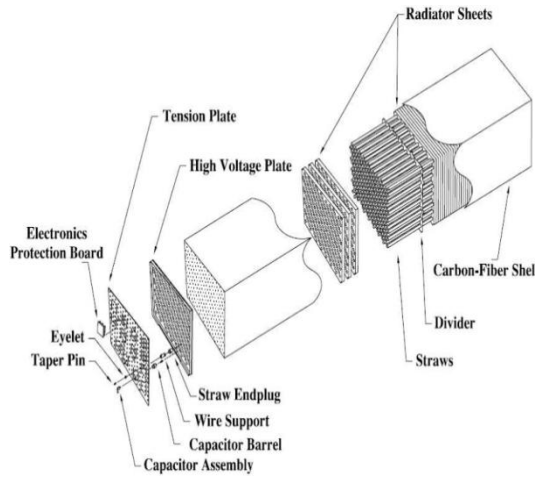


Figure 4.5. A view of a barrel module

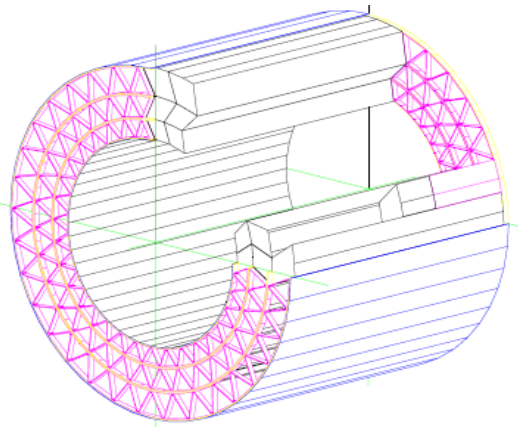


Figure 4.6. Layout of the barrel

showing a straw alignment plate, TRT showing three layers of barrel the straws, stacks of fiber radiator, modules (type I in the inner layer, and the shell.source [15] type II in the middle layer, and type III in the outer layer) and the support structure. Source [15]

The radiator chosen for the barrel consists of 5mm fabric plies, formed by polypropylene-polyethylene fibers, with a hole pattern to match the ones in the alignment planes. All the space in the shell between successive alignment planes is filled with radiator plies loosely packed. The straws, made from a coated polyimide film (Kapton based) and reinforced with C-fibers, are inserted through the holes and therefore totally embedded in the radiator.

The signal wire for the straws is a gold-plated tungsten wire with a $(30 \pm 0.3) \mu\text{m}$ diameter. The wires in the barrel TRT are electrically disconnected in the middle, with the exception of the nine most innermost layers, where the straw wires are divided in two places in order to give an active region of 36 cm at each end. The central part is not read out. This strategy reduces the occupancy of these straws, which otherwise would be too large for the proper operation of the detector in the

LHC environment. The wire sections are joined by fusing a small glass capillary tube to the two segments of wire. The wire is supported at the center of the straw by a wire centering structure, called twister. Twisters are also used for centering the wire at the end of each module.

4.6. End-cap wheels

Wheel production in Russia is making good progress despite some serious delays with some of the components (figure 4.7). Ten 4-plane wheels (out of a total of 80) have been delivered to CERN and undergone acceptance tests, namely dimensional, wire-tension, gas-tightness and high-voltage measurements as well as detailed gain mapping of each straw. The first 8-plane wheel has been prepared and will be used to begin the end-cap stacking procedure. As mentioned above, the gas-gain uniformity at each straw is inspected in an X-ray apparatus (Fig. 2, right). Through the gain scan, various straw characteristics can be assessed, such as the straightness of the straws or the gas-flow uniformity. The measurements, performed over $\sim 30,000$ straws, have shown that more than 99.9% of all straws are within the specifications.

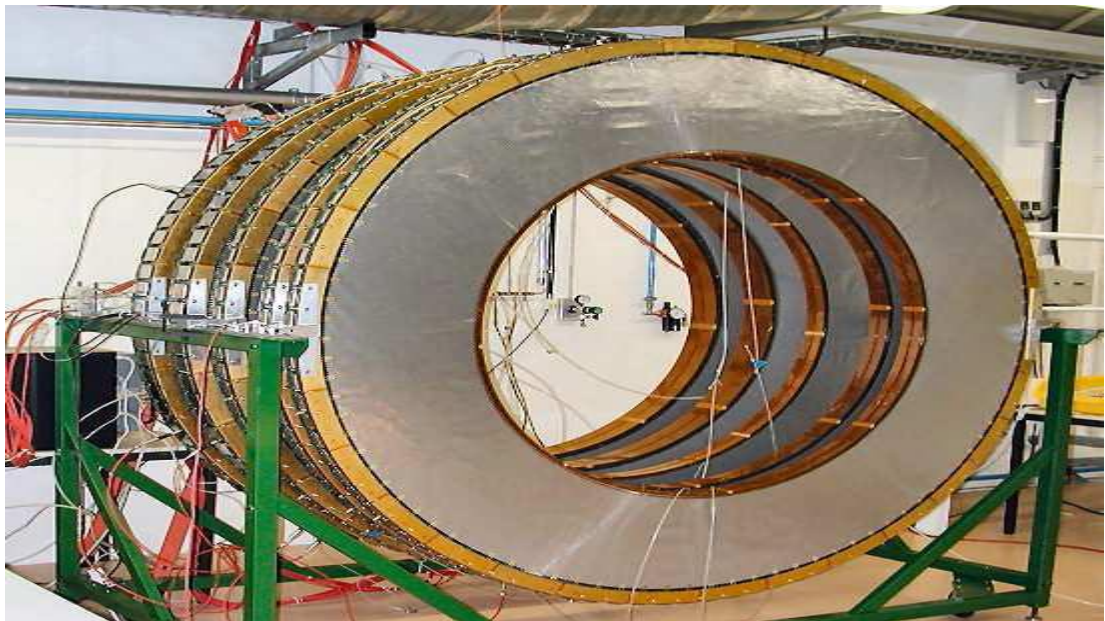


Figure 4.6. High voltage test stand with several end-cap wheels under high voltage.
Source[18]

CHAPTER 5

5. Particle Identification With The TRT

Transition-radiation photons, as described in the section above, are emitted at very small angle, and are therefore detected in the same straw as the ionizing particle. The absorption of the TR-photon in the straw gas gives rise to a very large point-like energy deposition. This highly-energetic cluster reaches the front-end electronics superimposed on the the usually lower-energy clusters due to track ionization. Very large energy depositions due to δ -rays constitute the main background to TR measurements. The front-end electronics was designed in order to tag a TR-photon candidate by discriminating the straw signal at a high-threshold, namely 5 keV, which is optimized for e/π separation using the cluster-counting technique.

5.1.Cluster-counting technique

Particle identification studies based on the cluster-counting technique with different TRT prototypes have been reported in [19, 20, 21]. In these studies, e/π separation was achieved by counting the number of high-threshold hits along the reconstructed track. For electrons, the tail above 5 keV is dominated by transition-radiation hits, while for pions it is mostly due to δ -rays. By requiring more than a certain number of high-threshold hits along the track, the probability to misidentify pions as electrons was measured as a function of the electron efficiency. The performance of this technique is shown in Fig. 5.1, as measured in a test-beam with an end-cap sector prototype, using 20GeV pion and electron beams. The pion misidentification probability is shown as a function of the electron efficiency, while in the top left-hand corner the probabilities to observe a given number of high-threshold hits are shown.

The application of this technique for the ATLAS detector is illustrated in Fig. 5.2,

where a display of a simulated $B_d^0 \rightarrow J/\psi K_S^0$ event (at low luminosity) in the ATLAS barrel TRT is shown, and in Fig. 5.3, where portions of a pion track from the K_S^0 decay and of an electron track from a J/ψ decay are shown in an enlarged frame. Dots represent straws crossed by charged particles. The electron track contains obviously many more high-threshold hits (larger points) than the pion track.

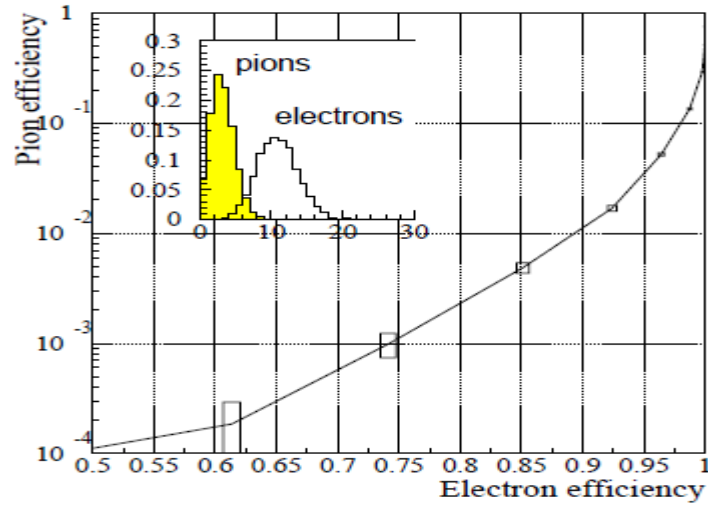


Figure 5.1. Pion misidentification probability as a function of the electron efficiency at 20GeV, as measured using an end-cap sector prototype. The probabilities to observe a given number of TR-clusters for pions and electrons are shown in the top left-hand corner. source [4]

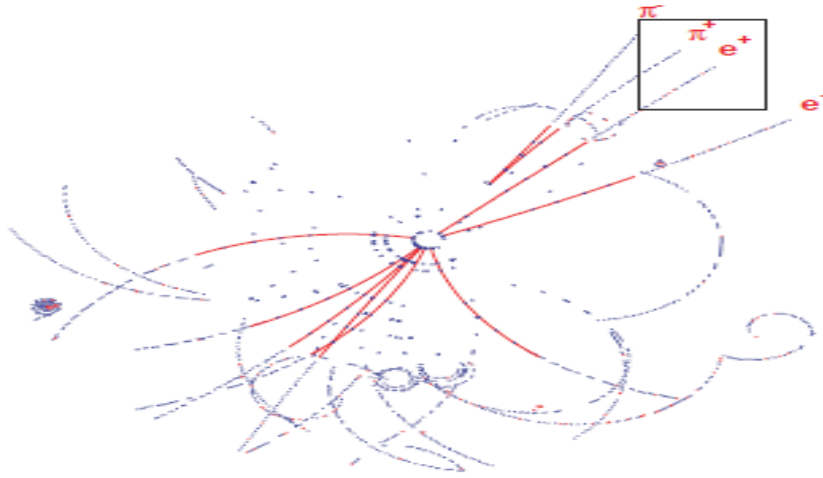


Figure 5.2. Display of a simulated $B_d^0 \rightarrow J/\psi K_S^0$ event in the ATLAS barrel TRT at low luminosity. Reconstructed tracks are drawn as lines only up to a radius of 50 cm so as not to obscure the TRT hits. The small box selects a part of a pion track from the K_S^0 decay and of an electron track from a J/ψ decay. source [4]

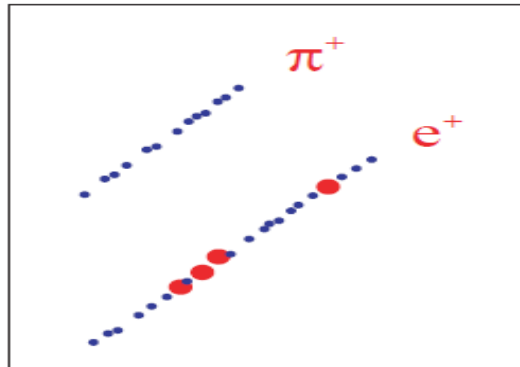


Figure 5.3. Expanded view of the portion of the tracks within the box in Fig. 5.2. The electron track contains many more high-threshold hits (larger points) than the pion track. Electron identification via transition radiation is based on this difference. source [4]

5.2. Time-over-threshold method

The low-threshold discriminator level is set to a nominal value of 200 eV, safely above the noise level ($\sigma \sim 40$ eV) and significantly below the average energy loss of ~ 2 keV, expected for minimum-ionizing particles traversing the straw gas. With this low-threshold setting, the front-end electronics was designed to detect the initial ionization cluster for precise drift-time determination.

The time-overthreshold [4] is defined as the width of the low-threshold discriminator signal. This signalwidth, larger for signals with larger amplitudes, contains partial information from dE/dx (not complete information since the signal is not integrated but just discriminated). The Bethe-Bloch curves, reported in Fig. 5.4 for particles in the TRT gas mixture,

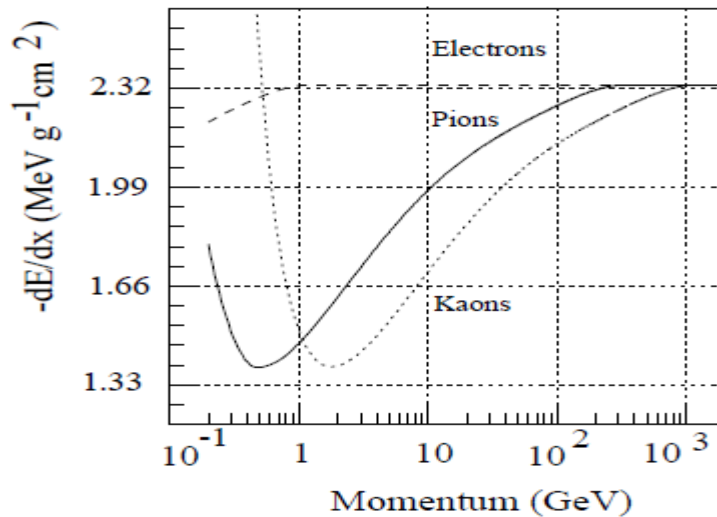


Figure 5.4. Bethe-Bloch curves for various particles in the ATLAS TRT gas mixture. For the energy range of interest for the TRT, electrons are always on the Fermi plateau, while hadrons are on the relativistic rise up to very large momentum. Source [4]

show that for the momentum range of interest at the LHC, electrons are always on the Fermi plateau, while hadrons are on the relativistic rise up to very large energy. As an example, a 10GeV electron will lose in the straw gas more energy than a 10GeV pion and therefore its time-over-threshold is expected, on average, to be greater.

However, the time-over-threshold also depends on the track position inside the straw

as illustrated in Fig. 5.5. For a track crossing the straw near the anode wire, the signal width is obviously larger than for the case when the track crosses the straw near the cathode. In order to extract information about the energy loss of a particle, it is important to correct for this dependence; this results in a significant improvement with respect to the method without track-position correction used in .

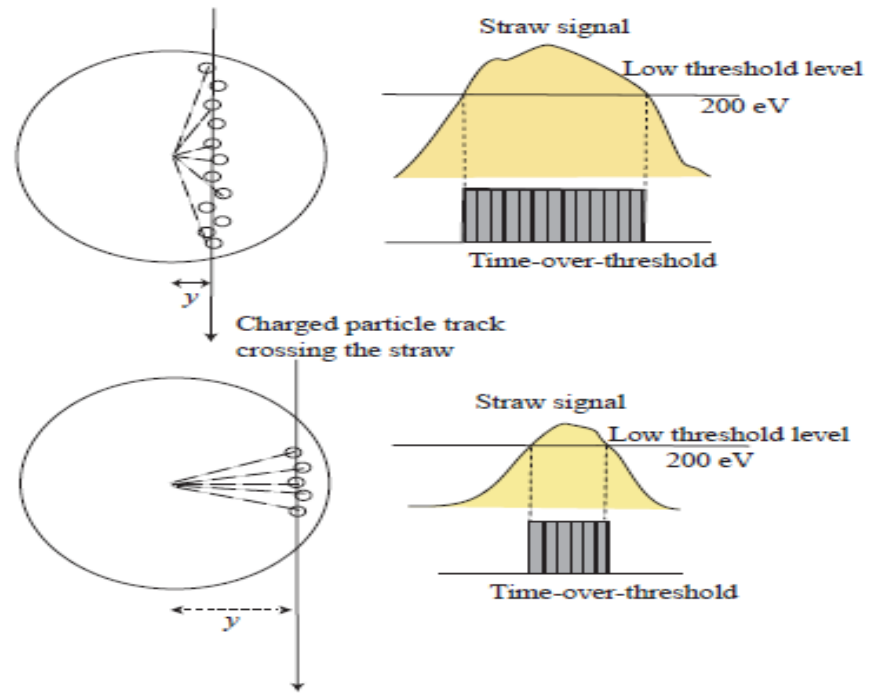


Figure 5.5. Dependence of the time-over-threshold on the track distance, y , from the wire. The straw signal is shown before and after the low-threshold (200 eV) discrimination. Source[4]

CHAPTER 6

6. PID Case Study: Dalitz Decay Of The Neutral Pion

6.1. Introduction

The π^0 meson has a mass of $135.0 \text{ MeV}/c^2$ and a short mean lifetime of $8.4 \times 10^{-17} \text{ s}$. This pion decays in an electromagnetic force process. The main decay mode, with probability 0.98798, is into two photons (two gamma ray photons in this case):

$$\pi^0 \rightarrow 2\gamma$$

Its second most common decay mode, with probability of 1.2%, is the Dalitz decay into a photon and an electron–positron pair as shown in Figure 6.1.

$$\pi^0 \rightarrow \gamma + e^- + e^+$$

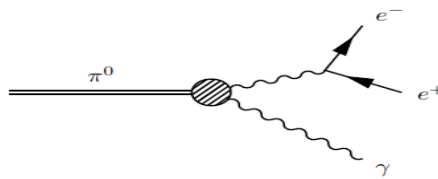


Figure 6.1. Pion decay mode

In this study, the Dalitz decay channel of neutral pion is selected using electron identification based on a simplified simulation of the TRT response to electrons and pions. A study of alternative treatments of high threshold information is performed to determine the most optimal approach to particle ID using the TRT detector.

6.2. Data

For the study, data is generated using the PYTHIA event generator (version 8.4). PYTHIA is a program for the generation of high-energy physics events, i.e. for the description of collisions at high energies between elementary particles such as e^+ , e^- , p and \bar{p} in various combinations. It contains theory and models for a number of physics aspects, including hard and soft interactions, parton distributions, initial- and final-state parton showers, multiple interactions, fragmentation and decay.

With PYTHIA configured to generate minimum-bias events from p-p collisions at 7 TeV center of mass, a total of 10 million events are generated and passed through a simple detector simulation called FAWP. The data file contains final state charged tracks and photons subject to the following cuts:

- pseudo-rapidity range $|\eta| < 2.5$
- charged transverse momentum $> 0.5 \text{ GeV}/c$
- photon energy $> 0.5 \text{ GeV}$

6.2.1. FAWP

FAWP (Fast Analysis with Pythia) is an analysis platform developed locally in the Gaziantep HEP group. It takes generator-level particles from PYTHIA, applies detector smearing, and presents to the researcher list of objects for easy processing.

In this simulation, the transverse momentum of charged tracks is smeared with a Gaussian sigma given by:

$$\sigma_{pT} = \sqrt{((0.05 \times pT) \times (0.05 \times pT) + 1.0)/100.0 \times pT} \quad (6.1)$$

Photon momenta are smeared with a Gaussian sigma given by:

$$\sigma_p = \sqrt{(0.01 \times p + 0.0001 \times p \times p)} \quad (6.2)$$

For each charged track, the number of TRT low-level hits, n_{lt} , is assigned randomly as follows:

$$n_{lt} = \text{int}(12.5 + 12 \times (\text{randFlat}() + \text{randFlat}() + \text{randFlat()})) \quad (6.3)$$

where $\text{randFlat}()$ is a function returning a uniformly distributed random value in the range $[0,1)$.

The distribution of low level hits is shown in Figure 6.2

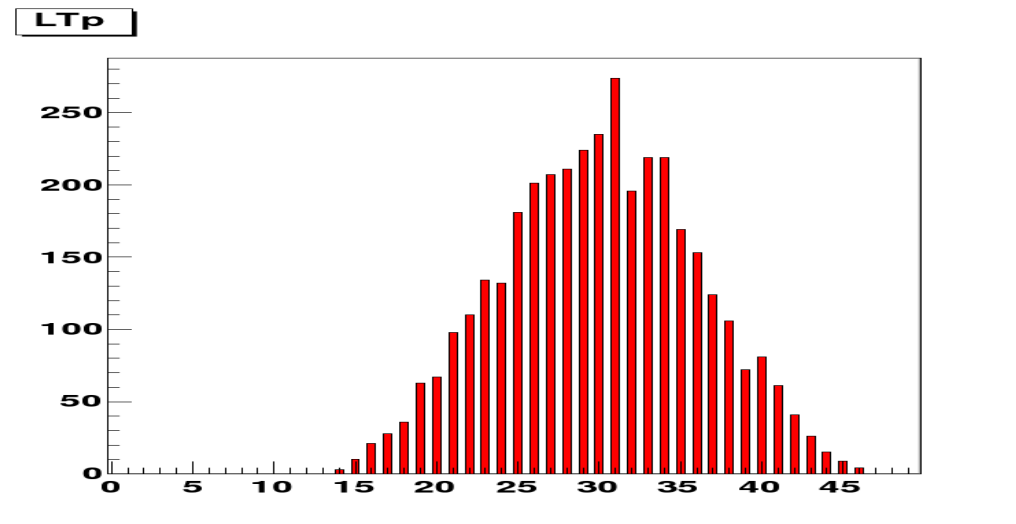


Figure 6.2. number of low level hits, n_{lt} , as simulated by FAWP.

Each hit is tested for a high-threshold with a high-threshold probability $p_{HT}(\gamma)$ given by:

$$p_{HT}(\gamma) = C_1 + \frac{C_2}{1.0 + \exp\left(-\frac{\log_{10}\gamma - C_3}{C_4}\right)} \quad \text{with} \quad \gamma \in [1, 500000] \quad (6.4)$$

where the parameters c_i are given in Figure 6.3.

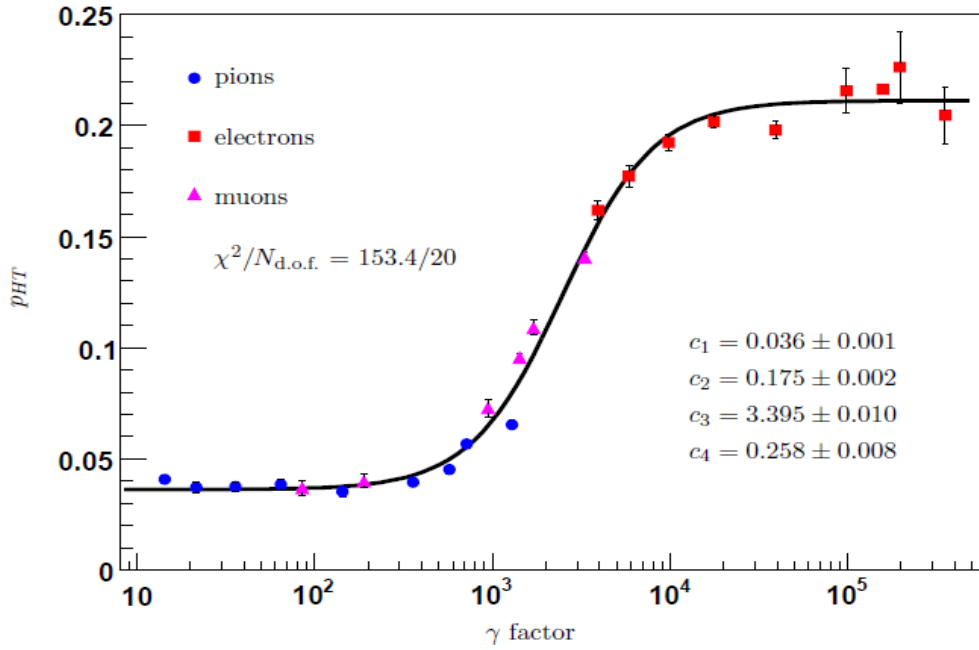


Figure 6.3. High threshold probability as a function of the gamma-factor. The curve is a fit to test beam data.

The distribution of high threshold hits for charged tracks is shown in Figure 6.4; here there is an equal number of electrons and pions. This distribution reveals the general behaviour for particles of different type and momentum present in p-p collisions where electrons and pions can be separated with the TRT.

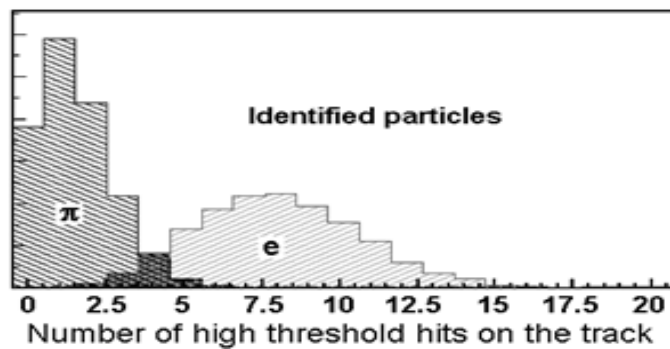


Figure 6.4. Distribution of the number of high threshold hits, n_{ht} , for pions and electrons in the FAWP simulation of the TRT with equal number of electrons and pion

6.3. Analysis

In practice, the number of pions is very much larger than the number of electrons. Figure 6.4 is replotted in Figure 6.5 using all charged tracks in the data. Here a

logarithmic scale is required to reveal the distribution for electrons against the large background of pions.

Clearly the high value tails from pions require a harder cut on nht to obtain a good electron purity, however this will result in a low electron efficiency.

In this study we will investigate the effect of cutting into distributions of nht on the reconstruction of the Dalitz decay of the neutral pion, and investigate alternative forms of the distribution in an attempt to optimise the performance of the TRT.

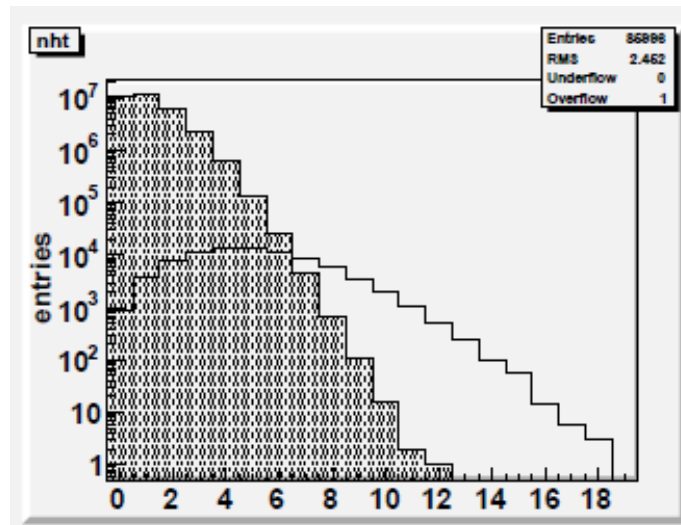


Figure 6.5. Distribution of the number of high threshold hits, nht, for pions and electrons.

An alternative to cutting directly on nht is to cut on the ratio of nlt/nht. This distribution is shown in Figure 6.6. One might expect this parameter to provide improved discrimination as the number of expected high threshold hits scales with the number of straw hits which varies from track to track (Figure 6.2).

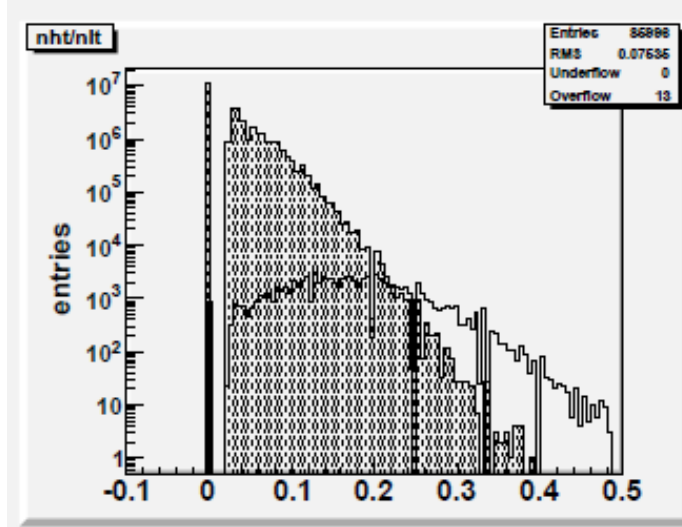


Figure 6.6. Distribution of the number of high threshold hits divided by the number of low threshold hits, n_{ht}/n_{lt} .

A second alternative is to form a chi value that takes into consideration the expected number of high level hits and the expected variation in the number of high level hits:

$$\gamma = \frac{E}{m} = \frac{\sqrt{p^2 + m^2}}{m} \quad (6.5)$$

$$\langle n_{ht} = n_{lt} * p_{ht}(\gamma) \rangle \quad (6.6)$$

$$\sigma_{ht} = \sqrt{n_{lt} * p_{ht}(1 - p_{ht})} \quad (6.7)$$

$$X^2 = \left(\frac{n_{ht} - \langle n_{ht} \rangle}{\sigma_{ht}} \right)^2 \quad (6.8)$$

The distribution of chi values for the same data is shown in Figure 6.7.

To study the relative performance of cutting on these three parameters, we reconstruct the Dalitz decay $\pi^0 \rightarrow \gamma + e^- + e^+$ with the electron candidates taken from the data with cuts on n_{ht} , n_{ht}/n_{lt} and χ . Making harder cuts on these parameters increases the electron purity while decreasing electron efficiency. To optimize the signal significance of the reconstruction of the Dalitz signal we are generally interested in maximizing both purity and efficiency, or in other word maximizing the product of purity and efficiency.

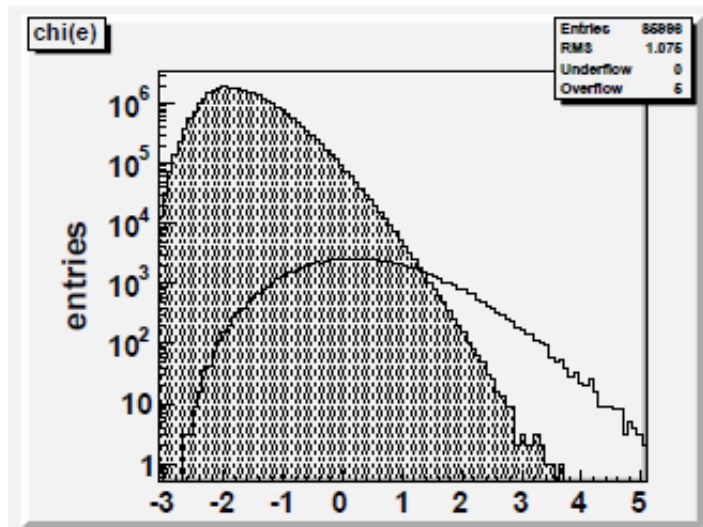


Figure 6.7. Distribution of chi

Figure 6.8 shows the Dalitz signal (black filled) and background (unfilled) for increasing values of n_{ht} . As the value of n_{ht} increases, the background reduces and the signal becomes clearer. For excessively hard cuts on n_{ht} the size of the signal diminishes resulting in a pure but statistically poor signal.

Figure 6.9 shows the same set of plots using cuts on n_{ht}/n_{lt} , and Figure 6.10 for cutting on χ . Purity and efficiency values and their products are shown in Figures 6.11, 6.12 and 6.13 for n_{ht} , n_{ht}/n_{lt} and χ respectively.

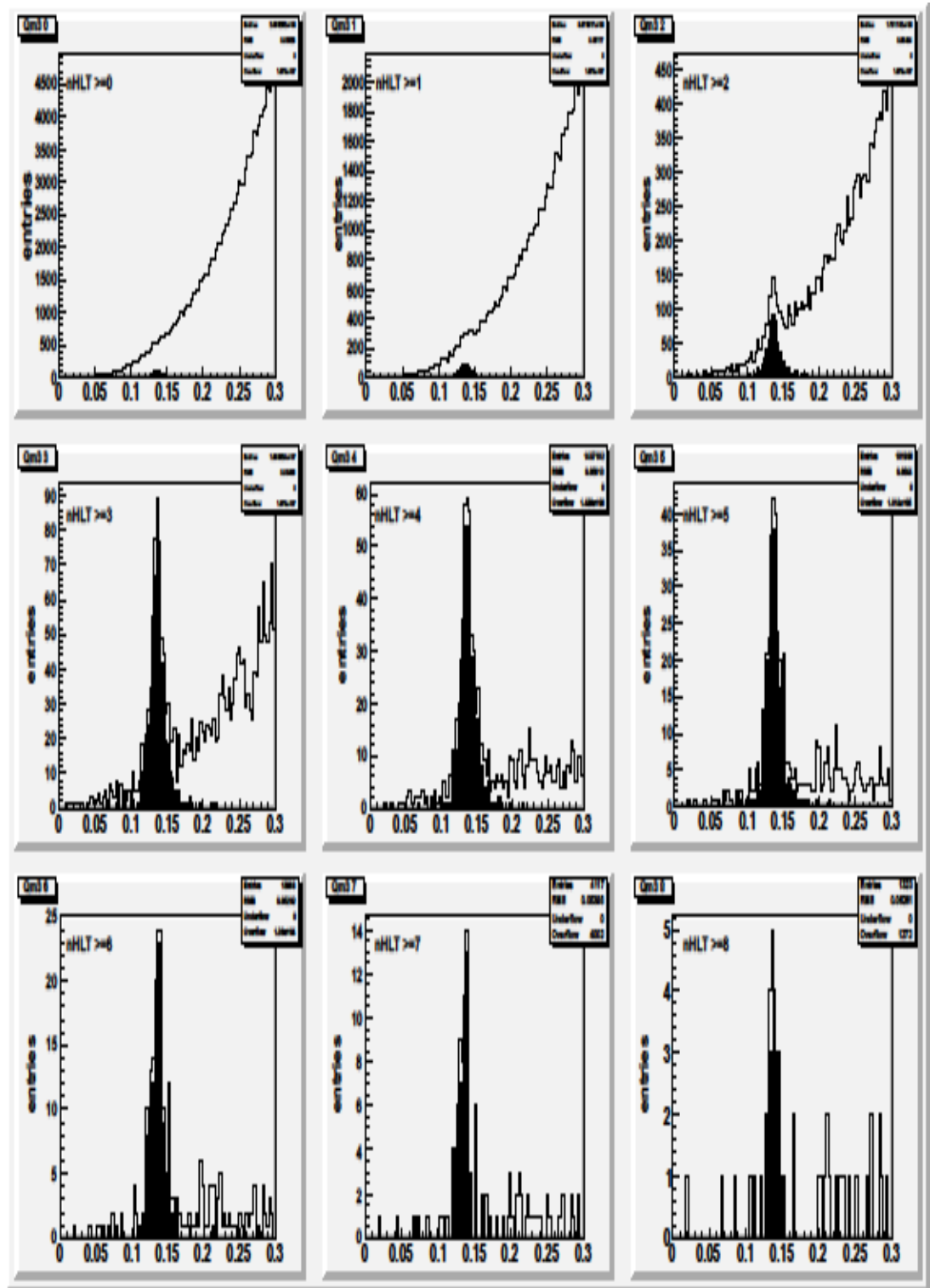


Figure 6.8. The reconstructed Dalitz signal with increasing cuts on n_{HLT}

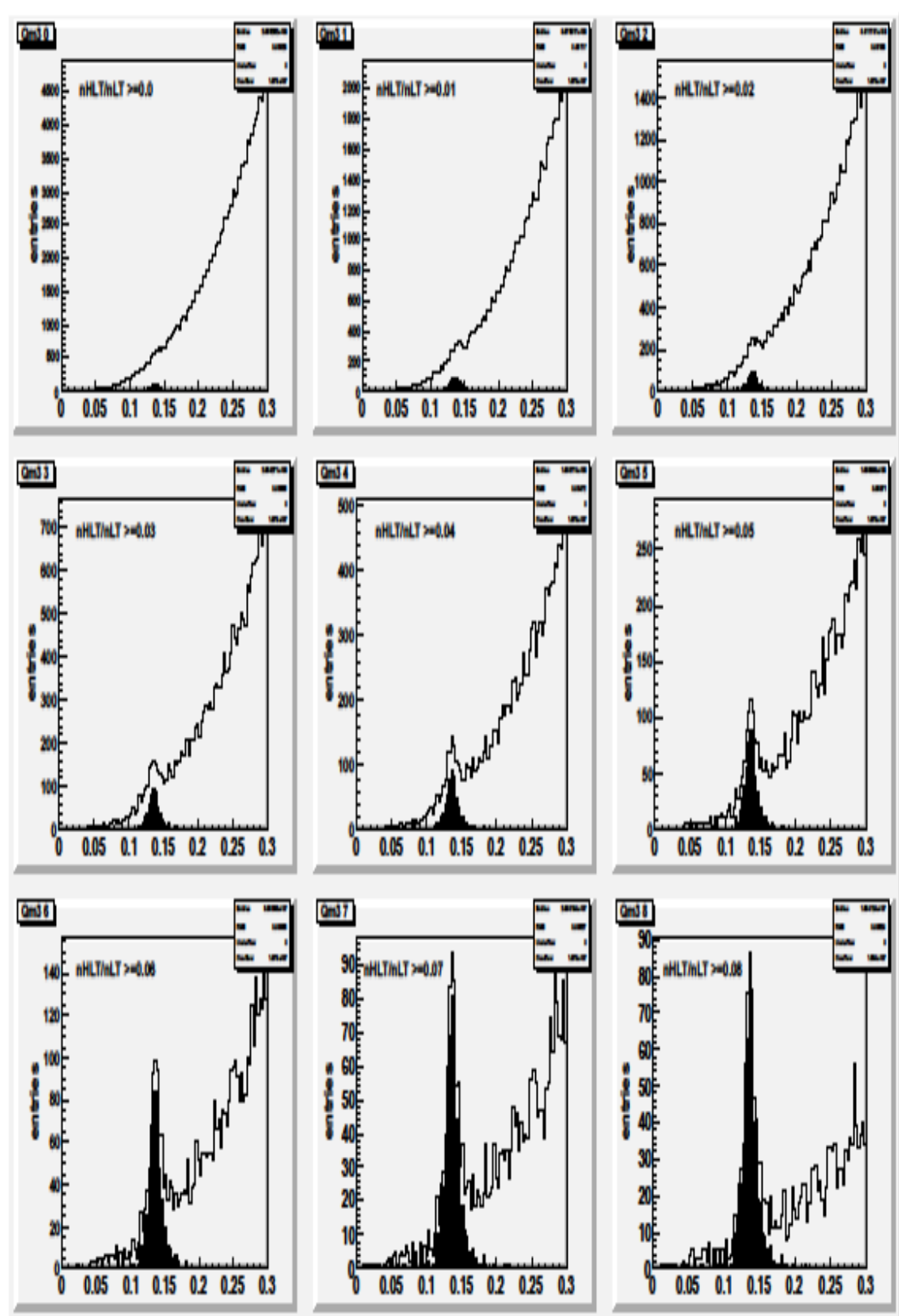


Figure 6.9. The reconstructed Dalitz signal with increasing cuts on n_{HL}/n_{LT} .

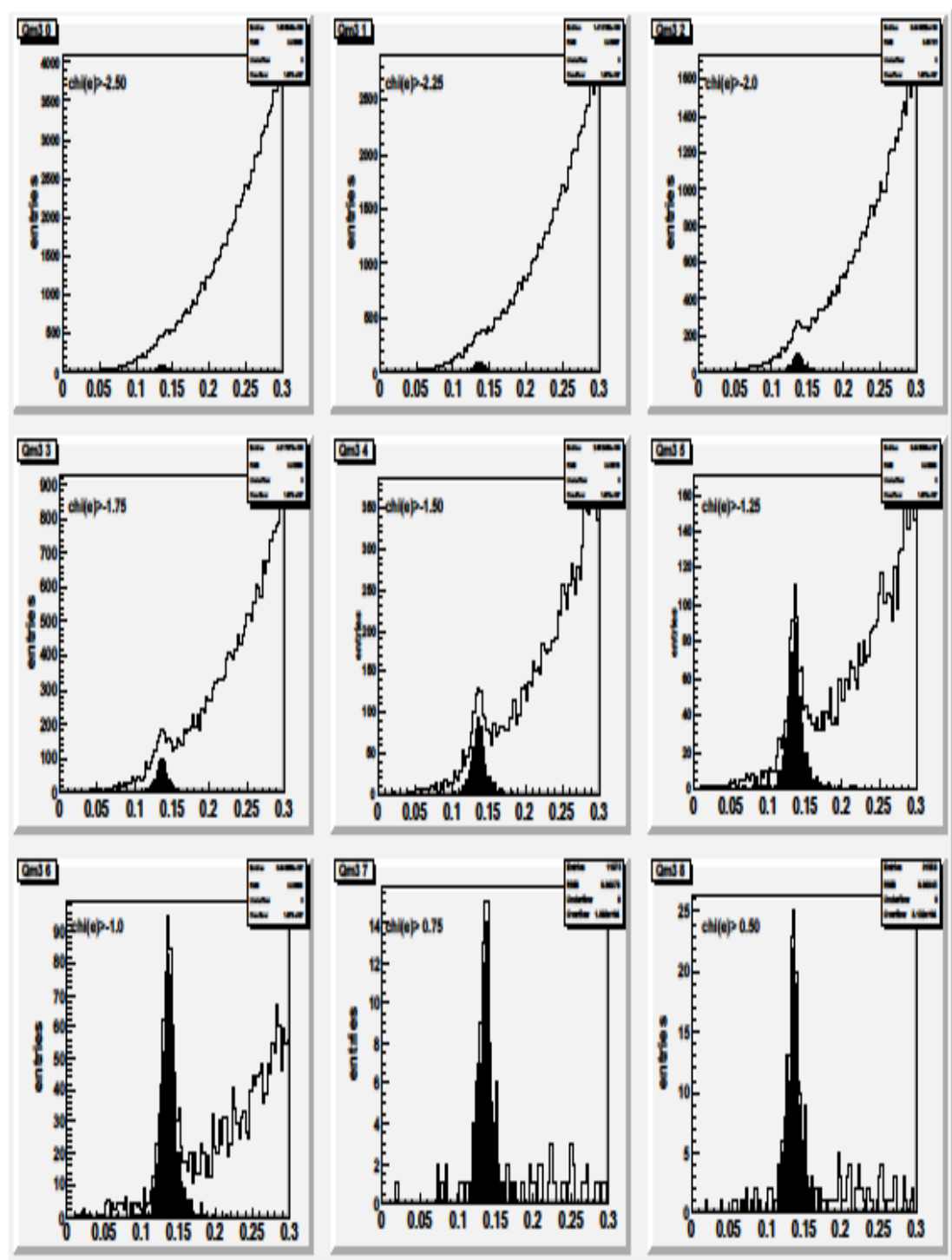


Figure 6.10. The reconstructed Dalitz signal with increasing cuts on χ .

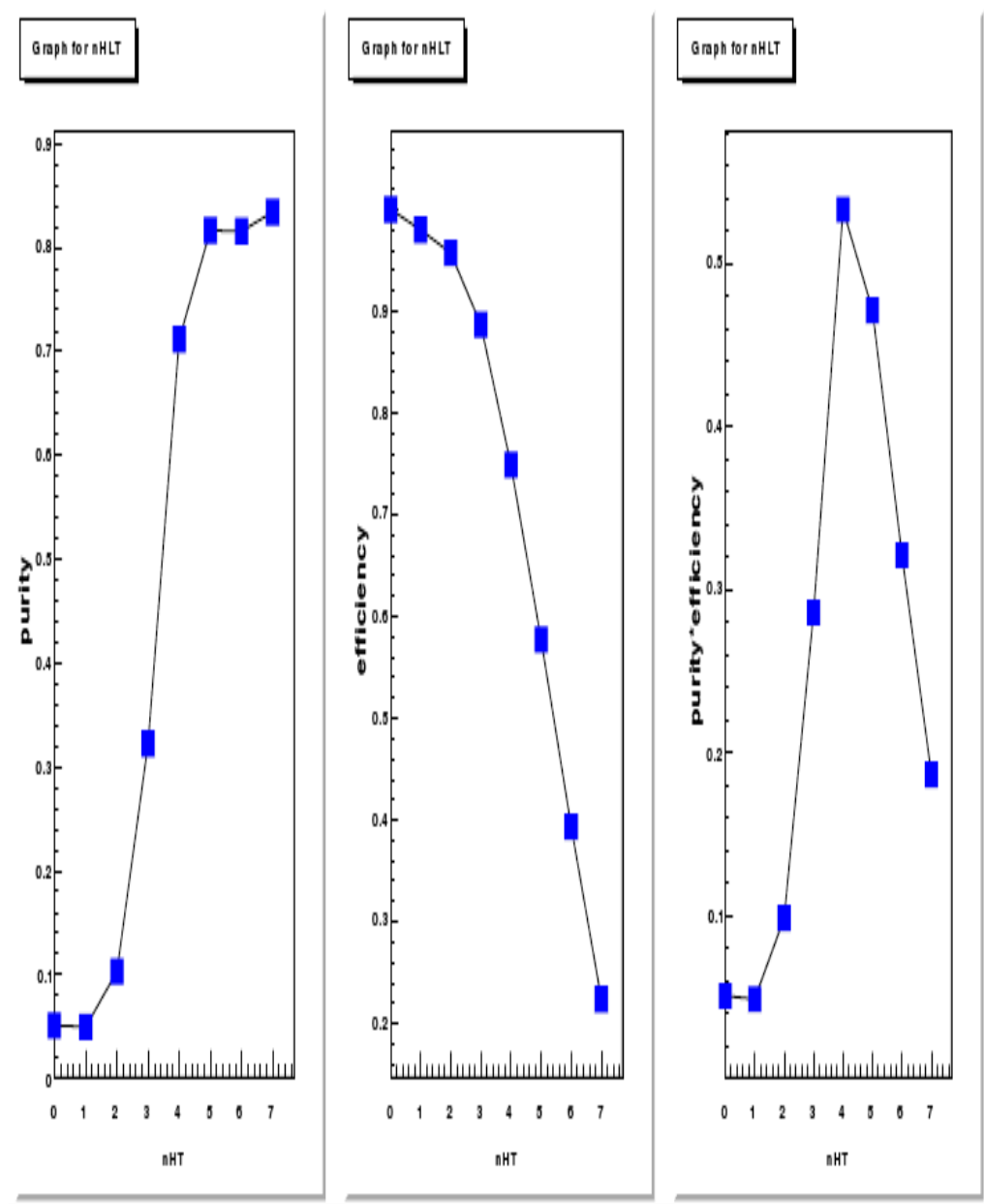


Figure 6.11. Purity, efficiency and their product for increasing cuts on nht.

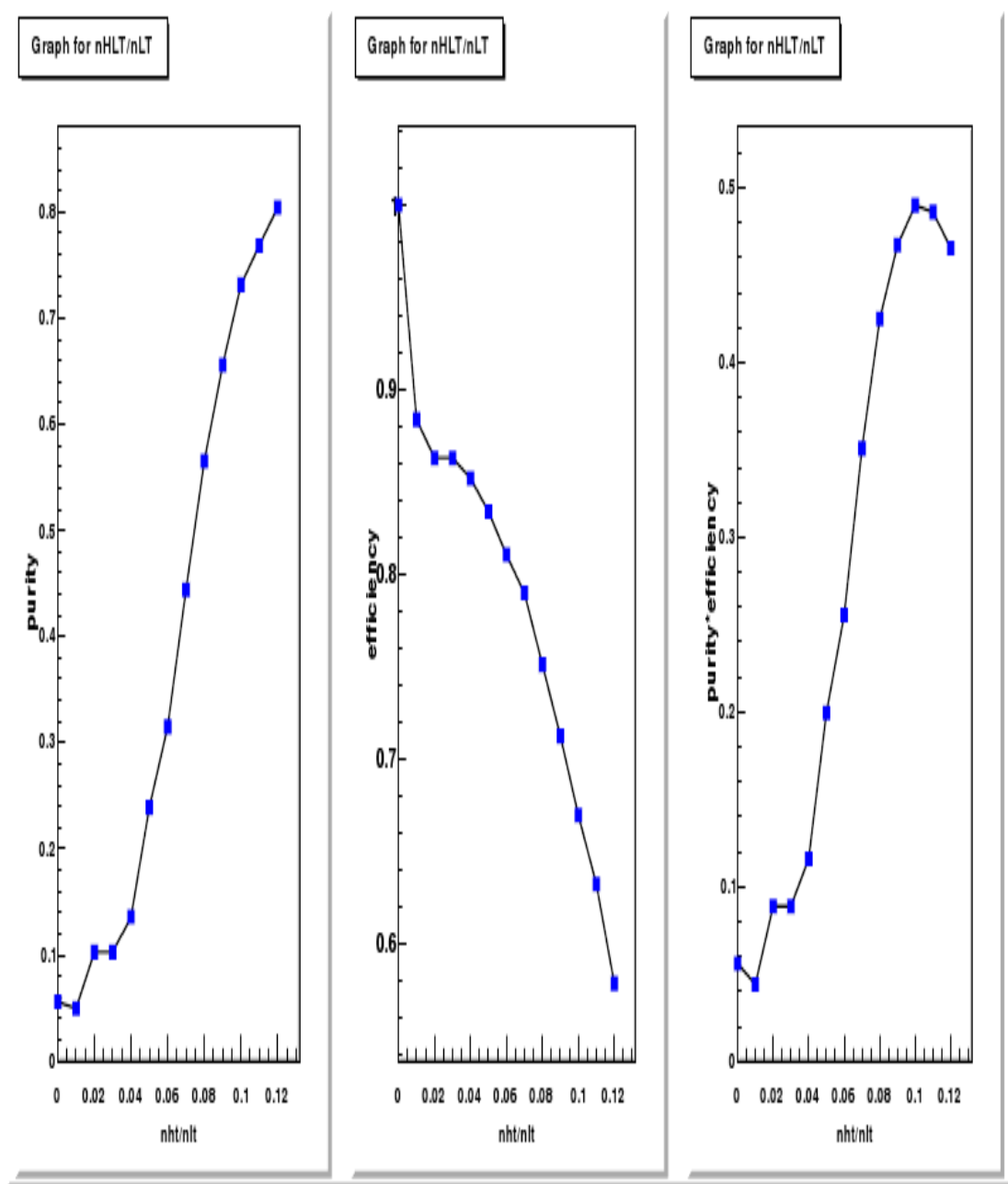


Figure 6.12. Purity, efficiency and their product for increasing cuts on nht/nlt.

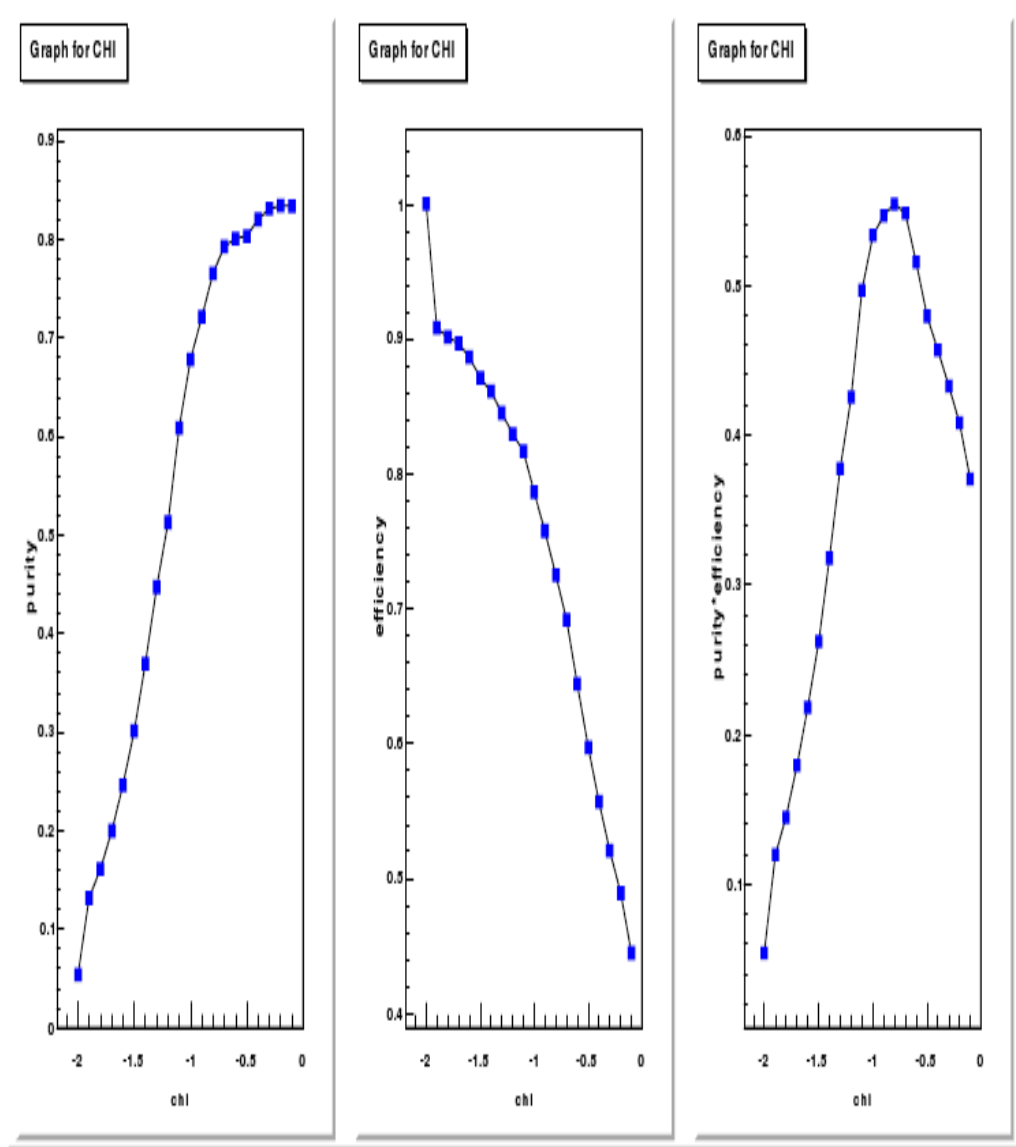


Figure 6.13. Purity, efficiency and their product for increasing cuts on chi.

From these results it is seen that an optimal value of efficiency time purity of about 0.52 is obtained with each cut method, the largest value of 0.56 is achieved with the chi method which also exhibits a smoother transition as the cut on chi increases.

CHAPTER 7

7. Summary And Conclusion

This study has shown the basic principles behind particle identification using the ATLAS TRT. A simulation of p-p collisions in environment of the LHC and subsequent simulation of the response of TRT straws shows that electrons and pions can be discriminated proving both pure and efficiency selection of electrons. A clear signal for the Dalitz decay of the pion can be reconstructed mostoptimally by cutting on a chi value (Equation 6.8).

This thesis compares three methods for the analysis electron-pion separation using the Transition Radiation Tracker in the ATLAS. We seen that the result of these three methods was nearly same.

REFERENCES

1. ATLAS Inner Detector Technical Design Report. (1997). *CERN/LHCC/97-17, ATLAS TDR 5*.
2. María Teresa Dova and the ATLAS Collaboration. (December 2009). The ATLAS experiment and its forward detector capabilities. *Nuclear Physics B - Proceedings Supplements*, **196**, 24-29
3. T. Akesson and the ATLAS Collaboration. (1 December 2001). Particle identification using the time-over-threshold method in the ATLAS Transition Radiation Tracker. *Nuclear Instruments and Methods in Physics Research Section A: Accelerators, Spectrometers, Detectors and Associated Equipment*, **474**,172-187
4. Andrea Manara.(October 2000).Particle identification using time-over-threshold measurements in the ATLAS Transition Radiation Tracker, *Nucl. Instr. and Meth. in Phys. Res. , A372*,75-137
5. L. Wartski et al., (August 1975). Interference phenomenon in optical transition radiation and its application to particle beam diagnostics and multiple-scattering measurements. *Journal of Applied Physics*. **46**, 3644-3653
6. R.G. Kepler (1960). Charge Carrier Production and Mobility in Anthracene Crystals. *Nucl. Instr. and Meth. in Phys. Res.* **119** ,4- 1226
7. R.G. Kepler (1960). Charge Carrier Production and Mobility in Anthracene Crystals. *Nucl. Instr. and Meth. in Phys. Res.* **119** 4- 1226
8. Cotter, Robert J. (1994). Time-of-flight mass spectrometry. *Columbus, OH: American Chemical Society*, 4 8412-3474.
9. Landau, L. D.; Lifshitz, E. M.; Pitaevskii, L. P. (1984). Electrodynamics of Continuous Media. *Cerenkov Radiation in Photonic Crystals*. **299**, 368
10. Amina Khan (31 March 2010). Large Hadron Collider rewards scientists watching at Caltech". Los Angeles Times. Retrieved 2010-04-02.
11. *CERN FAQ*. CERN Communication Group. (January 2008). *What is LHCb*. p. 13.

12. K. Aamodt *et al.* (ALICE collaboration) (2008). The ALICE experiment at the CERN LHC. *Journal of Instrumentation* **3**,8
13. Marcello Barisonzi. (2008, August 25-26). Detectors and Experimental Techniques. *Top Physics at ATLAS*. 4-22.
14. A. Augusto Alves Jr. *et al.* (LHCb Collaboration) (2008). The LHCb Detector at the LHC. *Journal of Instrumentation* **3**, 246
15. Esben Bryndt Klinkby. (2008). W mass measurement and simulation of the Transition Radiation Tracker at the ATLAS experiment. . *Instr. and Meth. in Phys. Res.*, 15-22
16. ATLAS Detector and Physics Performance. (May 1999). *Technical Design Report. Vol. 2*, CERN-LHCC-99-15.
17. V. A. MITSOU.(November 21, 2003). *The ATLAS Transition Radiation Tracker*. 2-5
18. ATLAS Collaboration.(2008). *The ATLAS TRT end-cap detectors*, JINST To be published
19. J. T. Shank *et al.* (1991). Ultrafast secondary emission X-ray imaging detectors: A possible application to TRD . *Nucl. Instr. and Meth. in Phys. Res.*, A310 -133.
20. T. Akesson *et al.* (1996). Electron identification with a prototype of the transition radiation tracker for the ATLAS experiment. *Nucl. Instr. and Meth. in Phys. Res.*, A372-70.
21. T. Akesson *et al.* (1998). Operation of the ATLAS Transition Radiation Tracker under very high irradiation at the CERN LHC . *Nucl. Instr. and Meth. in Phys. Res.*, A412-200.